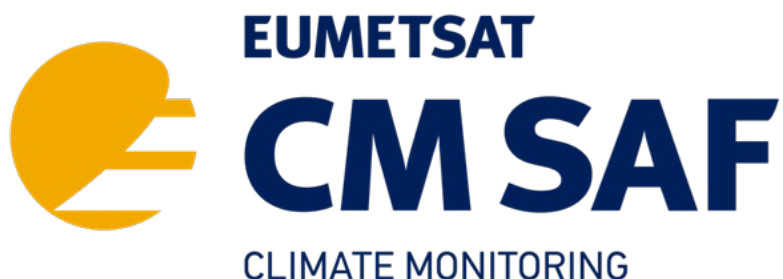


EUMETSAT Satellite Application Facility on Climate Monitoring



Algorithm Theoretical Basis Document Cloud Physical Products SEVIRI

	TCDR	ICDR
Cloud Phase (CPH)	CM-21043	CM-5041
Liquid Water Path (LWP)	CM-21053	CM-5051
Ice Water Path (IWP)	CM-21063	CM-5061

Reference Number:
Issue/Revision Index:
Date:

SAF/CM/KNMI/ATBD/SEVIRI/CP
3.3
08.08.2022

Document Signature Table

	Name	Function	Signature	Date
Author	Jan Fokke Meirink	CM SAF scientist		08/08/2022
	Nikos Benas	CM SAF scientist		
Editor	Marc Schröder	Science Coordinator		08/08/2022
Approval	CM SAF Steering Group			
Release	Rainer Hollmann	Project Manager		

Distribution List

Internal Distribution	
Name	No. Copies
DWD Archive	1
CM SAF Team	1

External Distribution		
Company	Name	No. Copies
PUBLIC		

Document Change Record

Issue/Revision	Date	DCN No.	Changed Pages/Paragraphs
1.0	02/10/2012	SAF/CM/KNMI/ATBD/SEVIRI/CP PP_1.0	Initial release prepared for DRI7
1.1	14/02/2013	SAF/CM/KNMI/ATBD/SEVIRI/CP PP_1.1	Revised version following DRI RIDs
2.0	28/04/2015	SAF/CM/KNMI/ATBD/SEVIRI/CP PP_2.0	Initial release for CLAAS edition 2 PCR

2.1	21/07/2015	SAF/CM/KNMI/ATBD/SEVIRI/C PP_2.1	Revised version following PCR RIDs
2.2	10/06/2016	SAF/CM/KNMI/ATBD/SEVIRI/C PP_2.2	Revised version following DRR RIDs
3.0	17/12/2020	SAF/CM/KNMI/ATBD/SEVIRI/C PP_3.0	Initial release for CLAAS edition 3 PCR. Summary of changes: <ul style="list-style-type: none"> - Inclusion of 3.8 μm processing - New products CDNC and CGT - Revised and extended uncertainty calculation - New surface albedo database - Changed cloud particle models for radiative transfer calculations - Various smaller updates
3.1	19/02/2021	SAF/CM/KNMI/ATBD/SEVIRI/C PP_3.1	Updates following PCR RIDs
3.2	x20/05/202 2	SAF/CM/KNMI/ATBD/SEVIRI/C PP_3_2	Updates for DRR/ORR: changes regarding ICDR
3.3	08/08/2022	SAF/CM/KNMI/ATBD/SEVIRI/C PP_3_3	Version after DR/ORR, with RID responses implemented

	Algorithm Theoretical Basis Document Cloud Physical Products SEVIRI	Doc. No: SAF/CM/KNMI/ATBD/SEVIRI/CP Issue: 3.3 Date: 08.08.2022
---	--	---

Applicable Documents

Reference	Title	Code
AD 1	EUMETSAT CM SAF CDOP 3 Product Requirements Document (PRD)	SAF/CM/DWD/PRD, 4.0

Reference Documents

Reference	Title	Code
RD 1	Algorithm Theoretical Basis Document: SEVIRI cloud products, CLAAS Edition 3	SAF/CM/CDOP3/DWD/ATBD/SEV/CLD, v3.2
RD 2	Algorithm Theoretical Basis Document for the Cloud Probability product of the NWC/PPS package	SAF/NWC/CDOP3/PPS/SMHI/SCI/ATBD/CloudProbability, v2.0d
RD 3	Algorithm Theoretical Basis Document for the Cloud Top Temperature, Pressure and Height of the NWC/PPS	SAF/NWC/CDOP3/PPS/SMHI/SCI/ATBD/CTTH, v3.0d
RD 4	Algorithm Theoretical Basis Document (An Appendix to the NWC/PPS) Cloud Probability and Cloud Top Temperature/Height from SEVIRI	SAF/CM/SMHI/ATBD/SEV/PPSSEV, v3.2
RD 5	Requirements Review, SEVIRI Edition 3 data records (CLAAS edition 3), Cloud products	SAF/CM/CDOP3/KNMI/RR37, v1.1
RD 6	RTTOV v11 Users Guide	NWPSAF-MO-UD-028, Version 1.3, 13/06/2014

Table of Contents

1	The EUMETSAT SAF on Climate Monitoring	8
2	Introduction	10
3	Algorithm Overview	12
3.1	Scientific Updates since CPP version 5.2	12
4	Algorithm description.....	13
4.1	Theoretical description.....	13
4.2	Radiative transfer.....	15
4.2.1	Infrared radiative transfer for cloud phase.....	15
4.2.2	VIS-IR radiative transfer for cloud optical properties	16
4.3	Retrieval scheme	22
4.3.1	Cloud phase	22
4.3.2	Cloud optical properties	24
4.4	Error budget estimates.....	25
4.5	Practical Application.....	31
4.5.1	MSG-SEVIRI instrument.....	31
4.5.2	Input data	32
4.5.3	Description of output.....	34
5	Assumptions and Limitations.....	36
6	Appendix	38
6.1	Surface albedo for TCDR.....	38
6.2	Surface albedo for ICDR.....	39
7	References.....	40
8	Glossary.....	45

List of Tables

Table 2-1: Overview of CM ^o SAF products covered in this ATBD and their respective TCDR and ICDR IDs.	10
Table 4-1: Properties of the cloudy atmosphere that are used for the radiative transfer calculations to generate the LUTs.....	19
Table 4-2: Typical magnitude of atmospheric correction, expressed as 1 minus the two-way transmissivity, in %. The numbers have been calculated for a reference atmosphere with $H_c = 2$ km, AMF = 2, TCO = 332 DU, and WVP = 30 kg m ⁻² , based on the MSG-SEVIRI spectral response, and for individual absorbing gases as well as for all gases together. Only the solar channels used for generating the CPP-SEVIRI dataset, i.e. channel 1 (0.6 μ m), channel 3 (1.6 μ m), and channel 4 (3.8 μ m), are presented here. The totals for all gases may differ somewhat from the sum of the individual gases because of rounding and saturation effects. For the 3.8- μ m channel, the absorption of individual gases are presented additive to the N ₂ -continuum (since N ₂ could not be switched off in MODTRAN). This explains why CO ₂ has a relatively low impact for SEVIRI, even though it absorbs nearly all radiation between 4.2 and 4.4 μ m.	21
Table 4-3: Error sources taken into account for CPP retrieval uncertainty estimates.....	27
Table 4-4: Relative uncertainties (in %) in COT and CRE retrievals as a total and separated by error source. The numbers reflect the median uncertainties from a full disk worth of SEVIRI retrievals (7 March 2017, 14:00 UTC). Pixels for which the observations were outside the look-up table or the visible surface albedo was larger than 0.6 were excluded. Results are shown separately for the 0.6–1.6 μ m and the 0.6–3.8 μ m retrievals as well as for liquid and ice clouds. Rows with a grey background contain the main error sources, some of which have been further separated as shown in the rows with a white background. The total uncertainty and the individual error source contributing most to the total uncertainty are indicated in bold face.	28
Table 4-5: Overview of the SEVIRI channels operating at 3x3 km ² spatial resolution. Channels used by CPP are indicated in bold.	31
Table 4-6: CPP variables in level-2 files: name, description and units.	34
Table 4-7: CPP processing flag.....	35
Table 8-1: Explanation of abbreviations and acronyms included in this document.	45
Table 8-2: Explanation of terms used in this document.	46

List of Figures

Figure 4-1: Simulated top-of-atmosphere (TOA) reflectance spectra for a stratocumulus (water) cloud and a cirrus (ice) cloud, and the imaginary part of the index of refraction of water and ice. The simulations were made with the MODerate spectral resolution atmospheric TRANsmittance and radiance code (MODTRAN) at $\theta_0 = 45^\circ$, $\theta = 0^\circ$ and $\varphi = 0^\circ$. The reflectances are plotted as black lines, while the refractive indices are plotted as gray lines. 13

Figure 4-2: Comparison between scattering phase functions of the severely roughened aggregate solid column habit, imperfect (roughened) hexagons, perfect (smooth) hexagons, and water droplets. The wavelength is $0.64 \mu\text{m}$ and the effective radii are $12 \mu\text{m}$ for the water droplets and $10 \mu\text{m}$ for the ice crystals..... 17

Figure 4-3: Asymmetry parameter (left) and single scattering albedo (right) as a function of cloud particle effective radius for the aggregate solid column and imperfect hexagon habits as well as liquid cloud droplets. Results are shown for three wavelengths: 0.6 , 1.6 and $3.8 \mu\text{m}$ 18

Figure 4-4: DAK calculations of TOA reflectance at $0.6 \mu\text{m}$ versus $1.6 \mu\text{m}$ (left), and $3.8 \mu\text{m}$ (right) for clouds consisting of spherical water droplets (red curves) and roughened, aggregate solid ice columns (blue curves). The reflectances have been calculated over a black surface (albedo = 0). Solar and satellite angles are indicated in the plots. The vertically oriented lines represent lines of equal cloud optical thickness, while the horizontally oriented lines represent lines of equal particle size. Values of optical thickness and cloud particle effective radius are indicated in the plot. Note the different scaling of the vertical axis in both panels. 19

Figure 4-5: Dependence of COT and CRE uncertainties on COT and CRE of both liquid and ice clouds for the $0.6\text{--}1.6 \mu\text{m}$ retrieval. Uncertainties due to different error sources are shown separately. COT and CRE histograms are indicated by the grey lines. 29

Figure 4-6: As Figure 4 5, but for the $0.6\text{--}3.8 \mu\text{m}$ retrieval. 30

Figure 4-7: COT and CRE uncertainties as a function of solar zenith angle (left) and VIS surface albedo (right). COT and CRE histograms are indicated by the grey lines. 30

Figure 4-8: Spectral response functions (red) and transmissivity spectra in the corresponding wavelength ranges (black) for the SEVIRI shortwave channels 1 to 4. The (TOA to surface) transmissivity spectra were calculated with MODTRAN for a clear-sky MLS standard atmosphere at $\theta_0 = 45^\circ$ 32

	Algorithm Theoretical Basis Document Cloud Physical Products SEVIRI	Doc. No: SAF/CM/KNMI/ATBD/SEVIRI/ CPP Issue: 3.3 Date: 08.08.2022
---	--	---

1 The EUMETSAT SAF on Climate Monitoring

EUMETSAT has set up and operates a network of Satellite Application Facilities (SAFs) which together with the EUMETSAT central facilities constitute the EUMETSAT application ground segments for Meteosat Second Generation (MSG) and Eumetsat Polar System (EPS). The importance of climate monitoring with satellites was recognized in 2000 by EUMETSAT member states when they amended the EUMETSAT Convention to affirm that the EUMETSAT mandate is also to “contribute to the operational monitoring of the climate and the detection of global climatic changes”. Following this, EUMETSAT established within its SAF network a dedicated center, the SAF on Climate Monitoring (CM°SAF, <https://www.cmsaf.eu>).

The consortium of CM°SAF currently comprises the Deutscher Wetterdienst (DWD) as host institute, and the partners from the Royal Meteorological Institute of Belgium (RMIB), the Finnish Meteorological Institute (FMI), the Royal Netherlands Meteorological Institute (KNMI), the Swedish Meteorological and Hydrological Institute (SMHI), the Meteorological Service of Switzerland (MeteoSwiss), the Meteorological Service of the United Kingdom (UK MetOffice), and the Centre National de la Recherche Scientifique (CNRS) in France.

Since the beginning in 1999, the CM°SAF has developed capabilities for a sustained generation and provision of Climate Data Records (CDR’s) derived from operational meteorological satellites. In particular, the generation of long-term data records is pursued. The ultimate aim is to make the resulting data records suitable for the analysis of climate variability and potentially the detection of climate trends. CM°SAF works in close collaboration with the EUMETSAT Central Facility and liaises with other satellite operators to advance the availability, quality and usability of Fundamental Climate Data Records (FCDRs) as defined by the Global Climate Observing System (GCOS). As a major task the CM°SAF utilizes FCDRs to produce records of Essential Climate Variables (ECVs) as defined by GCOS. Thematically, the focus of CM°SAF is on ECVs associated with the global energy and water cycle.

Another essential task of CM°SAF is to produce data records that can serve applications related to the Global Framework of Climate Services initiated by the WMO World Climate Conference-3 in 2009. CM°SAF is supporting climate services at national meteorological and hydrological services (NMHSs) with long-term data records but also with data records produced close to real time that can be used to prepare monthly/annual updates of the state of the climate. Both types of products together allow for a consistent description of mean values, anomalies, variability and potential trends for the chosen ECVs. CM°SAF ECV data records also serve the improvement of climate models both at global and regional scale.

As an essential partner in the related international frameworks, in particular WMO SCOPE CM (Sustained COordinated Processing of Environmental satellite data for Climate Monitoring), the CM°SAF - together with the EUMETSAT Central Facility, assumes the role as main implementer of EUMETSAT’s commitments in support to global climate monitoring. This is achieved through:

- Application of highest standards and guidelines as lined out by GCOS for the satellite data processing,

	Algorithm Theoretical Basis Document Cloud Physical Products SEVIRI	Doc. No: SAF/CM/KNMI/ATBD/SEVIRI/Cpp Issue: 3.3 Date: 08.08.2022
---	--	--

- Processing of satellite data within a true international collaboration benefiting from developments at international level and pollinating the partnership with own ideas and standards,
- Intensive validation and improvement of the CM°SAF climate data records,
- Taking a major role in data record assessments performed by research organizations such as WCRP (World Climate Research Program). This role provides the CM°SAF with deep contacts to research organizations that form a substantial user group for the CM°SAF CDRs,
- Maintaining and providing an operational and sustained infrastructure that can serve the community within the transition of mature CDR products from the research community into operational environments.

A catalogue of all available CM°SAF products is accessible via the CM°SAF webpage, <http://www.cmsaf.eu/>.

2 Introduction

This CM^oSAF Algorithm Theoretical Basis Document (ATBD) provides detailed information on the retrieval algorithms that are used to derive cloud physical properties (CPP) from Meteosat Second Generation (MSG) Spinning Enhanced Visible and Infrared Imager (SEVIRI) measurements as part of the third edition of the CLOUD property dAtAset using SEVIRI (CLAAS) data record (CLAAS-3). Disseminated products are instantaneous, daily and monthly cloud thermodynamic phase (CPH), liquid water path (LWP) and ice water path (IWP). Table 2-1 shows the corresponding product numbers. CLAAS-3 consists of a TCDR (2004-2020) and an ICDR (2021-present), which have different product IDs, as indicated in the table. The TCDR and ICDR products are produced with nearly identical algorithms, with differences only in ancillary input data. Consequently, the contents of the cloud products are identical. The CPH product includes an extended cloud phase with more categories than liquid or ice. The LWP and IWP products contain as additional layers the cloud optical thickness (COT) and particle effective radius (CRE). Furthermore, the LWP product includes cloud droplet number concentration (CDNC) and cloud geometrical thickness (CGT) as extra layers.

Table 2-1: Overview of CM^oSAF products covered in this ATBD and their respective TCDR and ICDR IDs.

Product	TCDR ID	ICDR ID
CPH	CM-21043	CM-5041
LWP	CM-21053	CM-5051
IWP	CM-21063	CM-5061

The algorithm described in this document is originally based on Roebeling (2008) and Roebeling et al. (2006), but contains a wide range of modifications implemented since then. A first series of updates were introduced for the generation of CLAAS-1 (Stengel et al., 2014), and subsequent improvements were included in CLAAS-2 (Benas et al., 2017). CPP has also been applied to measurements from polar orbiting imagers, in particular AVHRR, to compile the CLARA data records, of which CLARA-A2 (Karlsson et al., 2017) is the latest release.

In this ATBD the current CPP version 6.0 is described, which will be used for the production of CLAAS-3. The description is restricted to level-2 (pixel level) retrievals; the methods used to aggregate level-2 data to daily and monthly products are outlined in [RD 1].

The cloud physical properties retrieval algorithm requires a cloud mask and cloud-top height and temperature as input. The algorithms for these products have been developed in the NWC SAF and are described in [RD 2] and [RD 3], while SEVIRI-specific details are covered in [RD 4]. The user requirements of the cloud products are presented in [RD 5] and also included in [AD 1].

In Section 3 an overview of the retrieval algorithms is presented. Section 4 gives a detailed description of the retrieval algorithms, consisting of the relevant underlying physics (Section 4.1), the radiative transfer modelling (Section 4.2), the implementation of the retrieval scheme

	Algorithm Theoretical Basis Document Cloud Physical Products SEVIRI	Doc. No: SAF/CM/KNMI/ATBD/SEVIRI/CPP Issue: 3.3 Date: 08.08.2022
---	--	--

(Section 4.3), the error budget of the retrieved products (Section 4.4), and the practical application of the algorithms (Section 4.5). Finally, assumptions and limitations are discussed in Section 5.

	<p style="text-align: center;">Algorithm Theoretical Basis Document Cloud Physical Products SEVIRI</p>	<p>Doc. No: SAF/CM/KNMI/ATBD/SEVIRI/ CPP Issue: 3.3 Date: 08.08.2022</p>
---	---	--

3 Algorithm Overview

The CPP (cloud physical properties) algorithm version 6.0 consists of two main parts. First, the cloud phase (CPH), representing the thermodynamic phase of particles near the top of the cloud, is determined from an extended cloud phase approach developed by NOAA's Clouds from AVHRR Extended (CLAVR-x) team. This algorithm consists of a series of threshold tests applied to observed and simulated infrared brightness temperatures.

The algorithm then proceeds with retrieving cloud optical thickness (COT or τ) and cloud particle effective radius (CRE or r_e), during daytime given the thermodynamic phase determined before. This retrieval scheme was developed at KNMI, first described in Roebeling et al. (2006), and is based on earlier methods that retrieve cloud optical thickness and cloud particle effective radius from satellite radiances at wavelengths in the non-absorbing visible and the moderately absorbing solar infrared part of the spectrum (Nakajima and King 1990; Nakajima and Nakajima 1995; Watts et al. 1998). Liquid and ice water path (LWP/IWP) as well as cloud droplet number concentration (CDNC) and cloud geometrical thickness (CGT) for liquid clouds are derived from COT and CRE.

3.1 Scientific Updates since CPP version 5.2

The main updates in CPP v6.0 since v5.2 that was used for the generation of CLAAS Edition 2 (Benas et al., 2017) are the following:

- Retrievals using the SEVIRI 3.9 μm channel have been enabled.
- New by-products Cloud Droplet Number Concentration (CDNC) and Cloud Geometrical Thickness (CGT) for liquid clouds have been introduced.
- The uncertainty estimates of all products have been revised and extended.
- The surface albedo database has been updated and improved.
- The radiative transfer look-up tables have been modified based on different choices for ice particle habits and size distribution and water droplet size distribution width.
- Several smaller algorithm updates have been implemented.

4 Algorithm description

4.1 Theoretical description

The principle of the CPP retrieval algorithm is that the reflectance of clouds at a non-absorbing wavelength in the visible region (VIS: 0.6 or 0.8 μm) is strongly related to the optical thickness and has little dependence on particle size, whereas the reflectance of clouds at an absorbing wavelength in the near-infrared region (NIR: e.g., 1.6 or 3.8 μm) is primarily related to particle effective radius. This feature allows the retrieval of COT and CRE from two channels of a passive imager. Moreover, Figure 4-1 shows that the imaginary parts of the refractive indices of water and ice, which are a measure for absorption, differ. For example, around 1.6 and 3.8 μm ice particles are more absorbing than water droplets. This feature, together with a series of spectral tests on the thermal infrared (IR) window channels is used to retrieve (daytime) cloud-top thermodynamic phase.

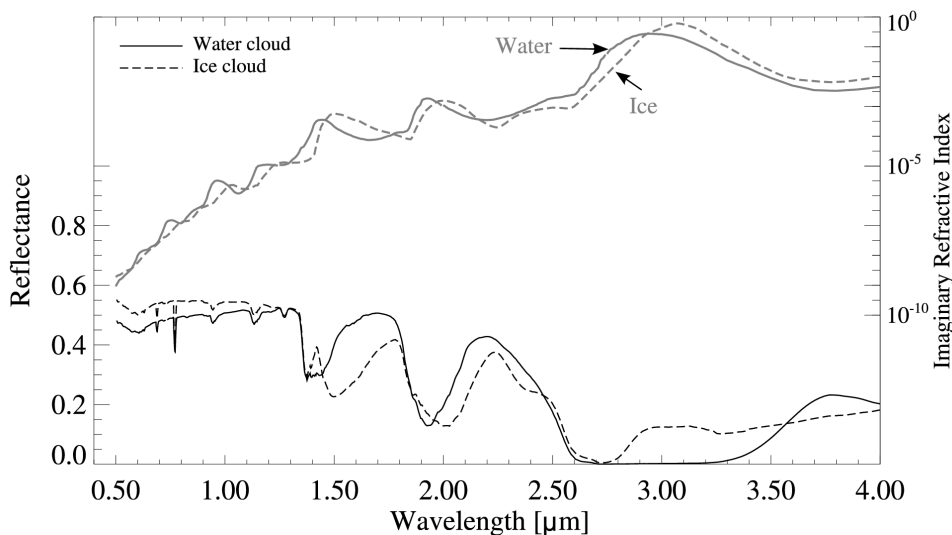


Figure 4-1: Simulated top-of-atmosphere (TOA) reflectance spectra for a stratocumulus (water) cloud and a cirrus (ice) cloud, and the imaginary part of the index of refraction of water and ice. The simulations were made with the MODerate spectral resolution atmospheric TRANsmittance and radiance code (MODTRAN) at $\theta_0 = 45^\circ$, $\theta = 0^\circ$ and $\varphi = 0^\circ$. The reflectances are plotted as black lines, while the refractive indices are plotted as gray lines.

The cloud optical thickness τ is defined at 0.6 μm under the assumption of a plane parallel atmosphere with reference to a vertical transect. The particle effective radius r_e is the relevant quantity for radiative scattering, and is given by the ratio of the mean particle volume to the mean projected cross-sectional area A (e.g., Schumann et al., 2011):

$$r_e = \frac{3V}{4A} \quad (1)$$

In case of a collection of spherical water droplets, this can be rewritten to:

$$r_e = \frac{\int_0^\infty r^3 n(r) dr}{\int_0^\infty r^2 n(r) dr} \quad (2)$$

where r is the droplet radius, and $n(r) dr$ is the number of particles per unit volume with radius between r and $r+dr$. Given the relatively small penetration depth into the cloud of photons at shortwave-infrared wavelengths, the retrieved effective radius reflects conditions near the cloud top.

The liquid water path (LWP) is calculated from τ and r_e assuming vertically homogeneous liquid water content (LWC), see e.g. Stephens (1978):

$$\text{LWP} = \frac{2}{3} \frac{2}{Q_e} \rho_l \tau r_e \quad (3)$$

where $\rho_l = 1.0 \times 10^3 \text{ kg m}^{-3}$ is the density of water and Q_e is the extinction efficiency at $0.6 \mu\text{m}$, which is approximated by its asymptotic value of 2 for cloud droplets that are large compared to visible wavelengths.

The liquid cloud droplet number concentration (CDNC or N_d) and liquid cloud geometrical thickness (CGT or H_g) can be determined from the retrieved τ and r_e following a model termed Idealized Stratiform Boundary Layer Cloud (ISBLC) by Bennartz et al. (2017). It assumes a (semi-)adiabatically stratified cloud with a linearly increasing LWC with height and a vertically constant CDNC. This model yields the following relations (see also Grosvenor et al., 2018):

$$H_g = \frac{2}{3} \left(\frac{5 \rho_l \tau r_e}{Q_e f_{ad} c_w} \right)^{\frac{1}{2}} \quad (4)$$

$$N_d = \frac{1}{2\pi k} \left(\frac{5 f_{ad} c_w \tau}{Q_e \rho_l r_e^5} \right)^{\frac{1}{2}} \quad (5)$$

where k is the third power of the ratio between volume mean radius and effective radius, which is set to 0.8, and c_w is the rate of increase in LWC with height for moist adiabatic ascent in kg m^{-4} (which is multiplied in (4) and (5) by the so-called adiabatic factor f_{ad} , set to 0.8, to obtain the actual rate of increase in LWC with height):

$$c_w = \rho_a \frac{c_p}{L_v} (\Gamma_m(T, P) - \Gamma_d) \quad (6)$$

where ρ_a is the air density, c_p is the specific heat of dry air at constant pressure, L_v is the latent heat of vaporization, and Γ_d and Γ_m are the dry and moist adiabatic lapse rates, respectively. The latter is a weak function of temperature and pressure, for which their values at the cloud top are taken.

Finally, Ice Water Path (IWP) is computed analogously to LWP assuming vertically homogeneous ice water content (IWC), leading to:

	Algorithm Theoretical Basis Document Cloud Physical Products SEVIRI	Doc. No: SAF/CM/KNMI/ATBD/SEVIRI/Cpp Issue: 3.3 Date: 08.08.2022
---	--	--

$$IWP = \frac{2}{3} \frac{2}{Q_e} \rho_i \tau r_e \quad (7)$$

where $\rho_i = 0.93 \times 10^3 \text{ kg m}^{-3}$ is the density of ice.

It should be noted that two different assumptions for the vertical profile of liquid water clouds have been employed. It was decided to adopt vertically homogeneous r_e and LWC in Eq. (3) for the calculation of LWP, consistently with the assumptions made in the radiative transfer simulations (see Section 4.2.2) and with those for ice clouds in Eq. (7). In contrast, the ISBLC model used for the calculation of CDNC and CGT is based on linearly increasing r_e and LWC with height. While stratocumulus clouds normally obey (sub-)adiabatic theory, leading to vertical profiles as in the ISBLC model, this is typically not the case for cumulus clouds, which tend to have a more uniform vertical profile (see Grosvenor et al., 2018 and references therein). Therefore, CDNC and CGT are more representative of the former cloud type, while LWP is more representative of the latter cloud type. Fortunately, the conversion of LWP from the homogeneous profile assumption to the adiabatic-cloud profile assumption is straightforward and only involves changing the factor 2/3 in Eq. (3) to 5/9, as outlined, for example, in Borg and Bennartz (2007).

A final remark is that since the ISBLC model assumes that r_e represents the effective radius at the cloud top, this model is only applied to retrievals using the 3.8- μm channel. Around that wavelength the photon penetration depth is very small (see also Platnick, 2001), making the retrieved r_e indeed sensitive to cloud droplet properties in a thin layer near the top of the cloud. Near 1.6 μm , cloud droplets are significantly less absorbing (see Figure 4-1), so photons penetrate deeper and the retrieved r_e represents droplets in a thicker layer below the cloud top.

4.2 Radiative transfer

In this section the radiative transfer calculations required to derive the cloud products are described, both for the cloud phase and for the cloud optical properties.

4.2.1 Infrared radiative transfer for cloud phase

The cloud phase algorithm needs cloudy-sky radiance profiles and clear-sky brightness temperatures as input in order to evaluate the measured brightness temperatures in the infrared. It was chosen to rely on the RTTOV algorithm [RD 6] to calculate these quantities. The used RTTOV version (11.3) has been developed within the NWP SAF. The model calculates radiances for satellite infrared or microwave nadir scanning radiometers based on atmospheric profiles of temperature, variable gas concentrations, cloud and surface properties. It takes into account absorption by gases including water vapour, ozone, carbon dioxide, nitrous oxide, methane and carbon monoxide, optionally based on vertical profiles provided by the user. The spectral range of the RTTOV v11 model in the visible/infrared is 0.4-20 μm with spectral models for a large number of supported platforms and sensors provided with the algorithm. All details on the radiative transfer algorithm and assumptions are provided in [RD 6].

	Algorithm Theoretical Basis Document Cloud Physical Products SEVIRI	Doc. No: SAF/CM/KNMI/ATBD/SEVIRI/ CPP Issue: 3.3 Date: 08.08.2022
---	--	---

The input to the RTTOV calculations are taken from grib files from European Centre for Medium-Range Weather Forecasts (ECMWF) analyses and/or short-term forecasts (see Section 4.5.2) regridded to the SEVIRI longitude-latitude grid using the Climate Data Operators (CDO: <https://code.zmaw.de/projects/cdo/wiki>) tool set. The required parameters entail vertical profiles of temperature, pressure and humidity, 2-meter values (temperature, wind, and humidity), skin temperature, and surface pressure. A standard atmosphere is used for other gases than water vapour. To reduce the computational time the RTTOV calculations are performed for blocks of 16x16 SEVIRI pixels, once for the surface type as specified in the RTTOV package (including monthly mean emissivity at 0.1 degrees spatial resolution) and once for water. These coarse-resolution calculations are then combined with a high-resolution land-sea mask in order to properly take into account the large contrast between the surface emissivity of water and other surfaces. Finally the satellite angles are used to enable the correct calculation of atmospheric extinction and transmission effects.

The two outputs used for the cloud phase calculation are:

- overcast radiance profiles: the level to space overcast radiance given by a black cloud for each level;
- clear-sky brightness temperatures (BT) corresponding to clear-sky TOA radiance.

These quantities are needed for SEVIRI channels 5, 7, 9, 10, and 11 (see Table 4-5). The outputs are written to an intermediate hdf file which is subsequently read by the cloud phase algorithm (Section 4.3.1).

4.2.2 VIS-IR radiative transfer for cloud optical properties

The CPP algorithm compares satellite observed reflectances at visible and near-infrared wavelengths to look-up tables (LUTs) of simulated reflectances for given cloud optical thicknesses, particle sizes and surface albedos for water and ice clouds. The Doubling Adding KNMI (DAK) radiative transfer model (RTM) has been used to generate the LUTs of simulated cloud reflectances. DAK has been developed for line-by-line or monochromatic multiple scattering calculations at UV, visible and near infrared wavelengths in a horizontally homogeneous cloudy atmosphere using the doubling-adding method (De Haan et al. 1987; Stammes 2001). DAK first calculates the reflection and transmission of an optically thin layer, in which no more than two scattering events may occur. Thanks to this restriction the radiative transfer equation can be solved analytically. Next, the reflection and transmission of two identical layers on top of each other can be obtained by computing successive reflections back and forth between the layers. This doubling procedure is continued until the actual optical thickness of the cloud is reached. The DAK model includes polarization. A pseudo-spherical correction is used as in Caudill et al. (1997). This correction accounts for attenuation of the solar beam as in a spherical atmosphere, while higher-order scattering is calculated for a plane-parallel atmosphere. DAK has been selected because it is the KNMI in-house shortwave RTM, and there is ample hands-on experience with this RTM at KNMI. Furthermore, comparisons with other RTMs have been performed, showing generally trustworthy results for DAK (Roebeling et al., 2005, see also Section 4.4).

Clouds are assumed to be plane-parallel and embedded in a multi-layered Rayleigh scattering atmosphere. The particles of water clouds are assumed to be spherical droplets with sizes following a two-parameter gamma distribution (Hansen, 1971). This distribution is described by the effective radius, varying between 3 and 34 μm , and the effective variance, set to 0.1. The latter value replaces an effective variance of 0.15 used in earlier CPP versions based on the findings of Benas et al. (2019) and references therein, that narrower size distributions lead to reduced retrieval artifacts in glory (backscatter) viewing conditions and are in better agreement with some more recent in situ observations. Scattering properties were calculated with Mie theory.

For ice clouds, severely roughened compact aggregates of eight solid columns have been adopted (Yang et al., 2013; Baum et al., 2011), as is also used in the Moderate Resolution Imaging Spectroradiometer (MODIS) Collection 6 (MOD06 C6) algorithms (Platnick et al., 2017). This aggregate solid column habit replaces the imperfect (i.e., roughened), randomly oriented, hexagonal ice crystals in monodisperse size distributions (Hess et al., 1998) which were used in earlier CPP versions (incl. CLAAS-2). Effective radii between 5 and 60 μm are considered and size distributions have an effective variance of 0.1. The scattering properties were obtained from Baum (2014).

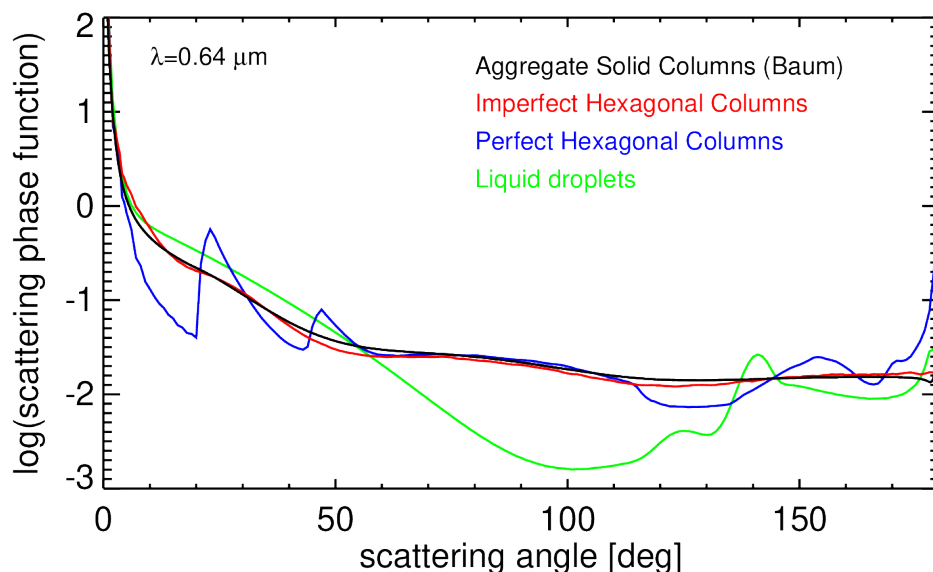


Figure 4-2: Comparison between scattering phase functions of the severely roughened aggregate solid column habit, imperfect (roughened) hexagons, perfect (smooth) hexagons, and water droplets. The wavelength is 0.64 μm and the effective radii are 12 μm for the water droplets and 10 μm for the ice crystals.

Scattering phase functions of water droplets and ice crystals are compared in Figure 4-2. For water droplets a strong reduction in sideways scattering is observed as well as enhanced scattering at the rainbow angle and in backscatter direction. Smooth ice crystals tend to yield distinct halo features and a strong backscatter peak. In contrast, roughened crystals show virtually featureless phase functions, and also yield considerably lower asymmetry parameters

compared to smooth crystals (Zhang et al., 2009). The imperfect hexagonal crystals and the aggregate solid columns yield quite similar phase functions, although there are differences, which are further illustrated in Figure 4-3 in terms of the asymmetry parameter g , and the single scattering albedo ω_0 . Changes in these properties have implications for the τ and r_e retrievals (see Platnick et al., 2017 for a discussion). The asymmetry parameter has decreased somewhat at all wavelengths with the new ice crystal model. A reduction in g at 0.6 μm leads to smaller retrieved τ because the quantity $\tau(1 - \omega_0 g)$ has been found to be invariant. The single scattering albedo has increased with the new ice habit. This lower absorption leads to higher simulated cloud reflectances at the absorbing wavelengths and thus larger retrieved r_e .

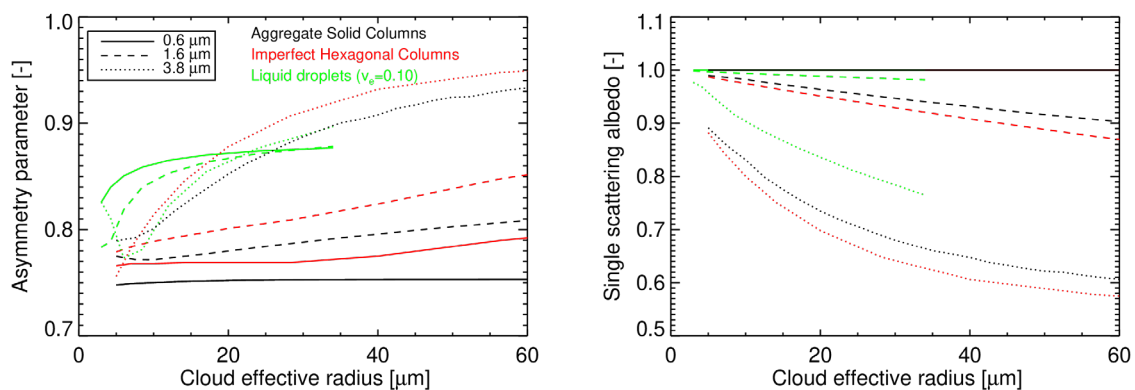


Figure 4-3: Asymmetry parameter (left) and single scattering albedo (right) as a function of cloud particle effective radius for the aggregate solid column and imperfect hexagon habits as well as liquid cloud droplets. Results are shown for three wavelengths: 0.6, 1.6 and 3.8 μm .

Figure 4-4 shows an example of DAK calculations of 0.6 and 1.6/3.8 μm reflectances as function of τ and r_e for water droplets and ice crystals. The figure illustrates that for optically thick clouds lines of equal τ and r_e are nearly orthogonal, meaning that the 0.6 and 1.6/3.8 μm reflectances contain independent information on τ and r_e , respectively. This is not the case for optically thin clouds. Moreover, for these clouds, the lines of different r_e are very close together, implying that the retrieval of particle size is inherently uncertain. The three NIR channels behave qualitatively similar but have different properties: broadly speaking the dynamical range in reflectance decreases towards longer wavelengths due to stronger absorption (Figure 4-1), while at the same time the lines of equal τ and r_e become orthogonal. Further, it is evident that ice clouds have lower 1.6- μm and 3.8- μm reflectances than water clouds, which is a consequence of the stronger absorption of ice particles compared to water droplets at these wavelengths (see Figure 4-1).

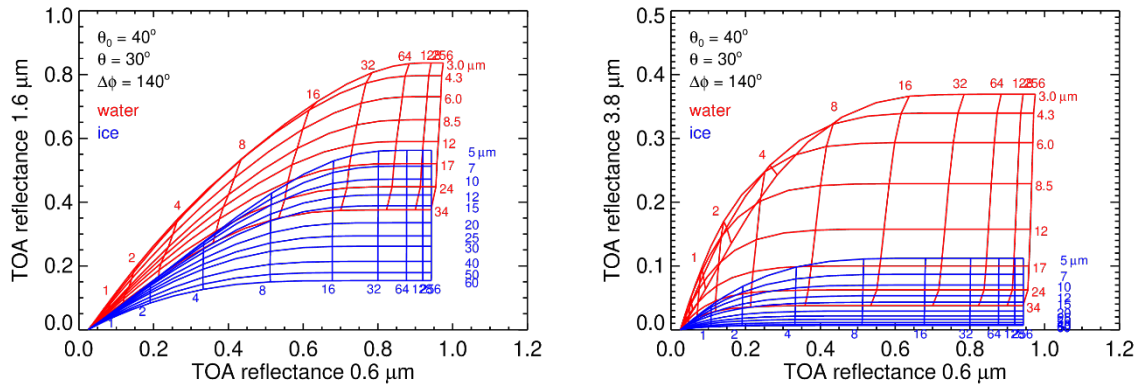


Figure 4-4: DAK calculations of TOA reflectance at 0.6 μm versus 1.6 μm (left), and 3.8 μm (right) for clouds consisting of spherical water droplets (red curves) and roughened, aggregate solid ice columns (blue curves). The reflectances have been calculated over a black surface (albedo = 0). Solar and satellite angles are indicated in the plots. The vertically oriented lines represent lines of equal cloud optical thickness, while the horizontally oriented lines represent lines of equal particle size. Values of optical thickness and cloud particle effective radius are indicated in the plot. Note the different scaling of the vertical axis in both panels.

Table 4-1: Properties of the cloudy atmosphere that are used for the radiative transfer calculations to generate the LUTs.

Parameter	Settings	
Vertical profiles of pressure, temperature, and ozone	Midlatitude summer ^{a)}	
Aerosol model	None	
Cloud height	Water clouds: 1000-2000 m; Ice clouds: 5000-6000 m	
Solar zenith angle (θ_0) ^{b)}	0 - 84.3° (73 Gaussian points in $\mu_0 = \cos(\theta_0)$)	
Viewing zenith angle (θ) ^{b)}	Same as θ_0	
Relative azimuth angle (ϕ) ^{b)}	0 - 180° (equidistant, 91 points)	
Cloud optical thickness	0 – 256 (equidistant in $\log(\tau)$, 22 points)	
	water clouds	ice clouds
Cloud particle type	Spherical water droplet	Roughened aggregate solid columns
Cloud particle size	3–34 μm equidistant in $\log(r_e)$, 8 points	[5, 7.5, 10, 12.5, 15, 20, 25, 30, 40, 50, 60 μm], 11 points
Liquid / Ice water path	0 – 4,836 g m^{-2}	0 – 9,523 g m^{-2}
Size distribution	Two-parameter gamma	Two-parameter gamma

Effective variance (v_e)	0.1	0.1
Complex refractive index	Segelstein (1981)	Warren and Brandt (2008)

^{a)} The midlatitude summer (MLS) atmosphere model was taken from Anderson et al. (1986). The choice of the temperature and pressure profile has a marginal impact on the LUT, namely only through Rayleigh scattering. Deviations from the MLS total column ozone are taken into account in the atmospheric correction procedure, see Eq. (9).

^{b)} The chosen distributions of angles are motivated in Wolters et al. (2006).

Table 4-1 summarizes the governing characteristics of the cloudy atmosphere, together with information about intervals of cloud properties and viewing geometries used in the DAK simulations to generate the LUT. The DAK simulations were done for a black surface. The TOA reflectance $R(\alpha_s)$ over a surface with reflectance α_s is computed using (Chandrasekhar, 1960):

$$R(\alpha_s) = R(\alpha_s = 0) + \frac{\alpha_s t_c(\theta_0) t_c(\theta)}{1 - \alpha_s \alpha_a} \quad (8)$$

Here, $t_c(\theta_0)$ and $t_c(\theta)$ are the cloud transmissivities at the solar and viewing zenith angles, respectively, and α_a is the hemispherical sky albedo for upwelling, isotropic radiation. The look-up table contains: $R(\alpha_s = 0)$ as a function of τ , r_e , θ_0 , θ , and ϕ ; t_c as a function of τ , r_e , and θ ; and α_a as a function of τ and r_e . The former two, $R(\alpha_s = 0)$ and t_c , are output of the DAK simulations, while α_a is determined from two additional DAK calculations with surface reflectance values of 0.5 and 1.0.

The DAK calculations concern monochromatic radiative transfer at a wavelength close to the centre of the respective satellite imager narrowbands. These calculations include Rayleigh scattering by air molecules and absorption by ozone at this wavelength, but neglect absorption by other atmospheric gases. Before the reflectance simulated by DAK can be compared to an observed reflectance, the absorption by atmospheric gases in the band has to be taken into account. This so-called atmospheric correction has been implemented based on MODTRAN4.2 (Berk et al. 2000) radiative transfer simulations. The atmosphere-corrected TOA reflectance ($R_{atm.corr.}$) is calculated as:

$$R_{atm.corr.} = R t_{a,ac}(\theta_0, H_c, WVP, TCO) t_{a,ac}(\theta, H_c, WVP, TCO) \quad (9)$$

where $t_{a,ac}$ is the above-cloud atmospheric transmissivity. Fixed (MLS) vertical profiles of water vapour and ozone are assumed, so that $t_{a,ac}$ becomes a function of the viewing or solar zenith angle, the cloud top height (H_c), water vapor path (WVP) and total column ozone (TCO). Absorption by trace gases within and below the cloud is neglected. The two-way transmissivity, i.e. the product of the two transmissivities in Eq. (9), is a function of the geometrical air mass factor ($AMF = 1/\mu_0 + 1/\mu$). This two-way transmissivity is in practice simulated by MODTRAN using a Lambertian surface, with arbitrary reflectance, placed at the cloud top height, and stored in a LUT with dimensions AMF, H_c , WVP, and TCO. An indication of the magnitude of the atmospheric correction is given in Table 4-2. The atmospheric correction depends on the exact spectral response of the specific instrument channels. For SEVIRI, absorption is particularly strong in channel 4 (see also Section 4.5.1), and it is crucial to take that accurately into account. Uncertainties in the retrievals caused by uncertainties in atmospheric correction – and the inputs needed for that – are further elaborated on in Section 4.4.

Table 4-2: Typical magnitude of atmospheric correction, expressed as 1 minus the two-way transmissivity, in %. The numbers have been calculated for a reference atmosphere with $H_c = 2$ km, AMF = 2, TCO = 332 DU, and WVP = 30 kg m⁻², based on the MSG-SEVIRI spectral response, and for individual absorbing gases as well as for all gases together. Only the solar channels used for generating the CPP-SEVIRI dataset, i.e. channel 1 (0.6 μm), channel 3 (1.6 μm), and channel 4 (3.8 μm), are presented here. The totals for all gases may differ somewhat from the sum of the individual gases because of rounding and saturation effects. For the 3.8-μm channel, the absorption of individual gases are presented additive to the N₂-continuum (since N₂ could not be switched off in MODTRAN). This explains why CO₂ has a relatively low impact for SEVIRI, even though it absorbs nearly all radiation between 4.2 and 4.4 μm.

Gas	Channel 1	Channel 3	Channel 4
O ₃	0.3 %	-	-
O ₂	0.2 %	-	-
H ₂ O	0.5 %	0.6 %	6.0 %
CO ₂	-	1.9 %	4.6 %
CH ₄	-	0.8 %	1.5 %
N ₂ O	-	-	3.4 %
N ₂	-	-	10.3 %
Total	1.0 %	3.4 %	25.5 %

More details on the implementation of atmospheric correction and the effect on retrieved cloud properties can be found in Meirink et al. (2009).

Whereas at 1.6 μm reflected sunlight is the only significant component of the measured TOA radiance, at 3.8 μm thermal emission by the surface, atmosphere and clouds provides a non-negligible contribution. Thermal emission is expressed as a reflectance (R_e), and calculated as the sum of contributions from surface ($R_{e,s}$) and cloud ($R_{e,c}$) following Nakajima and Nakajima (1995):

$$R_e = R_{e,s} + R_{e,c} = \left(\varepsilon_s B_\lambda(T_s) t_a(\theta) t_c(\theta) + \varepsilon_c B_\lambda(T_c) t_{a,ac}(\theta) \right) \frac{\pi}{\mu_0 F_{0,\lambda}} \quad (10)$$

where ε_s is the surface emissivity, T_s and T_c are the surface and cloud-top temperatures, respectively, $B_\lambda(T)$ is the Planck function at temperature T and wavelength λ ($= 3.8$ μm), $F_{0,\lambda}$ is the extraterrestrial solar flux at wavelength λ , and ε_c is the cloud emissivity approximated as:

$$\varepsilon_c = 1 - t_c(\theta) - R(\theta_0, \theta, \varphi). \quad (11)$$

ε_c is a function of τ and r_e through the cloud transmissivity t_c and reflectivity R . The retrieval procedure is the same as for the shorter-wavelength channels with the observed 3.8-μm

	Algorithm Theoretical Basis Document Cloud Physical Products SEVIRI	Doc. No: SAF/CM/KNMI/ATBD/SEVIRI/CPP Issue: 3.3 Date: 08.08.2022
---	--	--

radiance converted to a reflectance which is compared with the sum of simulated reflected sunlight and thermal emission.

4.3 Retrieval scheme

The CPP retrieval scheme consists of two parts. The first part is the retrieval of an extended cloud phase, and is described in Section 4.3.1. This extended phase is then reduced to two categories: liquid and ice. The second part is the retrieval of cloud optical properties (optical thickness and cloud particle effective radius) for the retrieved phase. This is further described in Section 4.3.2.

4.3.1 Cloud phase

The cloud phase retrieval is based on a number of threshold tests using SEVIRI observed as well as clear- and cloudy-sky simulated IR radiances and brightness temperatures. The algorithm is run for cloudy pixels and yields one of the following ‘extended’ cloud phase categories: liquid, supercooled, opaque ice, cirrus, overlap, and overshooting. The retrieval scheme follows developments by NOAA’s CLAVR-x team. Here, we provide a complete overview of the spectral tests and the order in which they are performed.

In this section the wavelength λ refers to the SEVIRI channels 4 (solar-thermal IR, 3.8 μm), 5 (water vapour, 6.3 μm), 7 (window, 8.7 μm), 9 (window, 11 μm), 10 (window, 12 μm), and 11 (CO₂, 13 μm), see also Table 4-5.

First, a number of quantities, which are used in the algorithm, are introduced. The effective emissivity ε_λ expresses the observed radiance L_λ relative to the radiance $L_{\lambda,\text{trop}}$ of a ‘cold reference’, being a black body at the tropopause height. It is defined by:

$$\varepsilon_\lambda = \frac{L_\lambda - L_{\lambda,\text{clr}}}{L_{\lambda,\text{trop}} - L_{\lambda,\text{clr}}} \quad (12)$$

where $L_{\lambda,\text{clr}}$ is the clear-sky radiance. The beta parameter $\beta_{\lambda_1-\lambda_2}$ (e.g., Heidinger and Pavolonis, 2009) is a measure of cloud microphysics, and is defined by:

$$\beta_{\lambda_1-\lambda_2} = \frac{\log(1 - \varepsilon_{\lambda_2})}{\log(1 - \varepsilon_{\lambda_1})} \quad (13)$$

It is mainly used to detect the presence of liquid water below ice clouds. In the 3.8- μm channel both solar reflection and thermal emission contribute to the observed radiance. A reflectance ($R_{3.8}$) is defined by using T_{11} to obtain a blackbody radiance, assuming an emissivity of one at 11 μm , and a zero transmissivity at 3.8 μm (implying $R_{3.8} = 1 - \varepsilon_{3.8}$), leading to (e.g., Pavolonis et al., 2005):

$$R_{3.8} = \frac{L_{3.8} - B_{3.8}(T_{11})}{F_{0,3.8\mu_0} - B_{3.8}(T_{11})} \quad (14)$$

	Algorithm Theoretical Basis Document Cloud Physical Products SEVIRI	Doc. No: SAF/CM/KNMI/ATBD/SEVIRI/ CPP Issue: 3.3 Date: 08.08.2022
---	--	---

where $B_{3.8}(T_{11})$ is the Planck function at wavelength $\lambda = 3.8 \mu\text{m}$ applied to the brightness temperature at wavelength $\lambda = 11 \mu\text{m}$, $F_{0,3.8}$ is the extraterrestrial solar flux in the 3.8- μm channel, and μ_0 the cosine of the solar zenith angle. Similarly, during nighttime, the emissivity is defined as:

$$\varepsilon_{3.8} = L_{3.8}/B_{3.8}(T_{11}) \quad (15)$$

The first step in the algorithm is the determination of an opaque cloud temperature T_c .

1. Using the water vapour channel

This method is only applied if the following checks for high clouds are fulfilled:

- a. $L_{6.3,\text{clr}} - L_{6.3} > 0.25$,
- b. $L_{11,\text{clr}} - L_{11} > 2.0$,
- c. $\text{COV}(T_{11}, T_{6.3}) > 1.0$, where COV denotes the covariance in the surrounding 5x5-pixel box.

A linear fit of the observed $(L_{11}, L_{6.3})$ against the simulated clear-sky $(L_{11}, L_{6.3})$ for the pixel under consideration is made. For a given layer, an overcast $L_{6.3}$ is then predicted applying the linear fit to the simulated overcast L_{11} . If this predicted overcast $L_{6.3}$ lies between the simulated overcast $L_{6.3}$ of the layer and the layer above, a match is found. T_c is set to the temperature of the lowest layer with such a match.

If no solution in this process is found or if the high-cloud checks are not fulfilled, indicating the cloud is low and opaque, the following method is used:

2. Using the 11- μm window channel

The observed L_{11} is compared with the simulated profile of overcast L_{11} . The profile is scanned from troposphere to surface until two adjacent layers are found for which the observed radiance is between the respective simulated overcast radiances. T_c is found by interpolation between the temperature of these layers.

Based on T_c (in Kelvin) an ice phase probability p_{ice} is calculated as:

$$p_{\text{ice}} = \text{MIN}(1, \text{MAX}(0, 1 - (T_c - 243)/20)).$$

Subsequently, a series of empirical tests for water and ice clouds are performed.

1. The phase is set to water ($p_{\text{ice}} = 0$) if one of the following holds. The physical meaning of (a) and (b) is that liquid clouds are more reflective (less emissive) than ice clouds; (c) is based on a difference in relative absorption in the 8.7 and 11 μm channels between ice and water.
 - a. Daytime ($\theta_0 \leq 84^\circ$): $p_{\text{ice}} > 0$ and $R_{3.8} > 0.2$ and $\varepsilon_{s,3.8} > 0.9$, where ε_s denotes the surface emissivity
 - b. Nighttime ($\theta_0 > 84^\circ$): $p_{\text{ice}} > 0$ and $\varepsilon_{3.8} < 0.95$.
 - c. $T_{8.7} - T_{11} < -1.0$.
2. The phase is set to ice ($p_{\text{ice}} = 1$) if the previous test did not yield water and one of the following cirrus tests is satisfied:
 - a. $T_{11} - T_{12} - F_{\text{WV}} > 1.0$, where

$$F_{WV} = 0.5, \text{ if } T_{11} \leq 265,$$

$$F_{WV} = (T_{11,ctr} - T_{12,ctr}) \frac{T_{11} - 260}{T_{11,ctr} - 260}, \text{ if } T_{11} > 265.$$

- b. $COV(T_{11}, T_{6.3}) > 1.5$ and $MAX(T_{6.3}) < 250$, where MAX denotes the maximum in the surrounding 3x3-pixel box.

The extended cloud phase is then determined as follows:

1. $p_{ice} \leq 0.5$
 - a. $T_c < 273 \rightarrow$ supercooled
 - b. $T_c \geq 273 \rightarrow$ water
2. $p_{ice} > 0.5$:
 - a. $T_c < 233 \rightarrow$ opaque
 - b. $T_c \geq 233$
 - i. $\epsilon_{11,tropo} < 0.8$
 1. $\beta_{11-12} < 0.95$ or $\beta_{11-13.4} < 0.7 \rightarrow$ overlap
 2. $\beta_{11-12} \geq 0.95$ and $\beta_{11-13.4} \geq 0.7 \rightarrow$ cirrus
 - ii. $0.8 \leq \epsilon_{11,tropo} \leq 0.95 \rightarrow$ opaque
 - iii. $\epsilon_{11,tropo} > 0.95 \rightarrow$ overshooting

The next step in the algorithm is a consistency check with the cloud-top temperature. Very cold clouds are not allowed to be liquid, and warm clouds are not allowed to be ice. Concretely, if the extended cloud phase is water or supercooled and $T_c \leq 231$ K, it is re-set to cirrus or opaque (if cloud optical thickness has been retrieved and is larger than 3). If the extended cloud phase is opaque, cirrus or overlap, and $T_c \geq 265$ K, it is re-set to water.

Subsequently, the extended phase is reduced to a cloud phase product, by setting the categories water and supercooled to liquid and the categories opaque ice, cirrus and overlap to ice. While during nighttime this is the final retrieved phase, during daytime this phase is the starting point of the optical properties retrieval process, through which it can still be modified if it turns out to be incompatible with the observed VIS-NIR reflectance pair. This is further explained in Section 4.3.2.

4.3.2 Cloud optical properties

For the cloud optical property retrieval, the observed VIS and NIR reflectances are compared with the simulated reflectances in the LUT. For the VIS reflectance the 0.6- μm channel is normally used. For the NIR reflectance, both the 1.6- or the 3.8- μm channel is used, resulting in two sets of CPP products.

In case the 3.8- μm channel is used as NIR channel, the observed radiance is expressed as a reflectance rather than a brightness temperature:

$$R_{3.8} = \frac{\pi L_{3.8}}{\mu_0 F_{0,3.8}} \quad (16)$$

which is then compared with the sum of simulated solar reflectance (from the DAK LUT) and thermal emission cast as a reflectance (from Eq. (10)). The cloud optical thickness and particle

	Algorithm Theoretical Basis Document Cloud Physical Products SEVIRI	Doc. No: SAF/CM/KNMI/ATBD/SEVIRI/ CPP Issue: 3.3 Date: 08.08.2022
---	--	---

size are retrieved in an iterative manner for cloudy pixels during daytime ($\theta_0 < 84^\circ$). During the iteration the retrieval of τ at the 0.6- μm channel is used to update the retrieval of r_e at the 1.6/3.8- μm channel, and vice versa. This iteration process continues until the retrieved cloud optical properties converge to stable values. The interpolation between cloud optical properties in the LUTs is done with cubic splines in τ for the smaller half of the τ -axis and in $\log(\tau)$ for the larger half of the τ -axis, while cubic splines in $\log(r_e)$ are applied for the whole r_e -axis.

If the observed reflectance pair is located outside the LUT space, the nearest solution at the border of the LUT space is reported. This is achieved by limiting τ and of r_e to their extreme values in the LUT axes in the iterative process described above. However, if the assigned phase is liquid and the observed reflectance pair lies 'below' (as in Figure 4-4) the liquid cloud LUT space, and if in addition the cloud top is not too warm (i.e. $T_c < 265$ K), the phase is reset to ice followed by a new $\tau - r_e$ retrieval attempt for an ice cloud. Similarly, if the assigned phase is ice and the observed reflectance pair lies 'above' the ice cloud LUT space, and if in addition the cloud top is not too cold (i.e. $T_c > 231$ K), the phase is reset to liquid followed by a new $\tau - r_e$ retrieval attempt for a liquid cloud. Via this mechanism the phase can be changed compared to what was described in Section 4.3.1, reflecting an important role of the NIR channel in the phase retrieval during daytime. If a phase switch occurs, the extended phase is adjusted accordingly: in the case of a switch from liquid to ice, the extended phase is re-set to cirrus (if $\tau \leq 3$) or opaque (if $\tau > 3$); in the case of a switch from ice to liquid, the extended phase is re-set to water.

4.4 Error budget estimates

The retrieval of cloud optical thickness and cloud particle effective radius from 2-channel backscattered solar radiation is a simple but heavily underconstrained problem. As a result, many uncertainties are associated to this retrieval problem (see Stephens and Kummerow (2007) for a review). In this section we first discuss a number of error sources which are not explicitly taken into account, and then explain the propagation of uncertainties that are taken into account, including in the observations and some of the ancillary data. Finally, a brief characterization of the resulting uncertainty estimates is given, focusing on the 0.6-1.6 and 0.6-3.8 μm channel retrievals.

To assess errors in forward radiative transfer modelling, Roebeling et al. (2005) compared three RTMs that use different methods to solve the equation of radiative transfer to a Monte Carlo model (Macke et al., 1999). Apart from DAK, used for the radiative transfer calculations underlying CPP, the Spherical Harmonics Discrete Ordinate Method (SHDOM: Evans 1998) and MODTRAN 4v2r0 (Berk et al., 2000), in which the multiple scattering calculations are based on the Discrete Ordinate (DISORT) method (Stamnes et al. 1988), were tested. In this analysis, DAK and SHDOM were found to agree rather closely over a range of cloudy cases, with a standard deviation of about 2% compared to the Monte Carlo model, but also an unexplained bias of about 3%. MODTRAN showed somewhat larger deviations, which were probably related to the preliminary status (beta release) of the version that was used. Differences between the RTMs depend on cloud properties as well as solar and viewing angles and since there is no real reference it is not possible to truly quantify the errors. Therefore, in

CPP the uncertainties related to radiative transfer are neglected for the estimation of retrieval uncertainties.

The comparisons described before were performed for idealized, plane-parallel, vertically homogenous, single-layer, single-phase clouds. These assumptions are usually violated, giving rises to potentially very large retrieval errors. They are discussed in more detail in Section 5, but are not taken into account in the uncertainty estimates. It should further be noted that no uncertainty is associated to the cloud phase retrieval, and that its impact on the cloud optical and microphysical properties uncertainty is also neglected. Now we turn our attention to the error sources that are taken into account and how uncertainty estimates are derived from them.

The following relation, which is the same as used in optimal estimation but in absence of a *priori* information (Rodgers, 2000), is applied to obtain the covariance matrix of retrieval uncertainties \mathbf{S}_r :

$$\mathbf{S}_r = \mathbf{K}^{-1} \mathbf{S}_y (\mathbf{K}^{-1})^T + \sum_i (\mathbf{K}^{-1} \mathbf{K}_{b_i}) \mathbf{S}_{b_i} (\mathbf{K}^{-1} \mathbf{K}_{b_i})^T \quad (17)$$

The first term describes the propagation of observation errors, where \mathbf{S}_y (2x2, diagonal) is the observation error covariance matrix. \mathbf{K} is the (2x2) Jacobian matrix containing the partial derivatives of TOA reflectance in each channel with respect to the retrieval variables τ and r_e . It is approximated from the gradients in the LUT. The second term describes the propagation of model errors. It is a summation over the different model / ancillary data error sources (e.g., water vapour path), where \mathbf{S}_{b_i} are the corresponding error covariance matrices. In our case, all error sources are assumed to be independent, and all \mathbf{S}_{b_i} are 1x1 matrices. The 2x1 matrices \mathbf{K}_{b_i} contain the partial derivatives of the simulated reflectance in each channel with respect to the particular error source. Only the (square root of the) diagonal elements of \mathbf{S}_r , denoted σ_τ and σ_{r_e} , are reported in the CPP output.

The LWP/IWP (here combinedly denoted by CWP), CDNC and CGT uncertainties can be calculated by propagating the uncertainties in COT and CRE in Eqs. (3), (4), (5) and (7):

$$\frac{\sigma_{\text{CWP}}}{\text{CWP}} = \frac{\sigma_\tau}{\tau} + \frac{\sigma_{r_e}}{r_e} \quad (18)$$

$$\frac{\sigma_{N_d}}{N_d} = 0.5 \frac{\sigma_\tau}{\tau} + 2.5 \frac{\sigma_{r_e}}{r_e} \quad (19)$$

$$\frac{\sigma_{H_g}}{H_g} = 0.5 \frac{\sigma_\tau}{\tau} + 0.5 \frac{\sigma_{r_e}}{r_e} \quad (20)$$

An overview of the error sources considered is given in Table 4-3. Specification of the uncertainties in the driving parameters approximately follows Platnick et al. (2017). For the reflectances, the bulk of systematic errors is thought to have been removed by careful calibration (Meirink et al., 2013). Here, the uncertainty is assumed to be 3% for all channels. The impact of uncertainties in several ancillary datasets is also quantified. Surface albedo is assumed to have a 15% (relative) uncertainty in all channels. As discussed in Section 4.2, atmospheric absorption is influenced by the total ozone column, water vapour path and cloud

top height, which are assigned relative uncertainties of 15%, 10% and 20%, respectively. Thermal emission, relevant in the 3.8- μm channel, depends mainly on surface temperature and cloud top temperature, while the parameters determining atmospheric absorption (except ozone, which does not play a role at 3.8 μm) also contribute. The surface temperature uncertainty is assumed to be 1.5 K. The cloud top temperature uncertainty is related to the cloud top height uncertainty on the basis of a lapse rate of 6.5 K km^{-1} . The cloud top height and temperature uncertainties are specified in a generic way based on results of validation with active instruments (Håkansson et al., 2018), rather than adopting the uncertainties associated with the pixel-level retrieval products used as input.

Table 4-3: Error sources taken into account for CPP retrieval uncertainty estimates.

Error source	Parameter	Specification
Observations	Reflectance VIS and NIR	3% (relative)
Land/ocean reflectance	Surface albedo VIS and NIR	15% (relative)
Atmospheric absorption	Total column ozone	15%
	Water vapour path	10%
	Cloud top height	20%
Thermal emission (3.8 μm)	Surface temperature	1.5 K
	Cloud top temperature	6.5 ΔCTH (K)

An indication of the magnitude of the estimated uncertainties and the contribution of the different error sources is given in Table 4-4. Note that these numbers were derived from MSG-SEVIRI retrievals. They should be very similar for AVHRR, although small differences will be caused by the different spectral response functions of the respective channels. The main error source for the COT retrieval is the visible reflectance. For CRE, the picture is more diverse. In case of the 0.6–1.6 μm channel combination, the NIR reflectance plays the main role. However, the VIS reflectance is also important, contributing about as much to the total uncertainty as the NIR reflectance, at least for liquid water clouds. This can be explained by the non-orthogonality of the LUT, especially for thin clouds. In case of the 0.6–3.8 μm channel combination, the correction for thermal emission and atmospheric absorption, for which uncertainties are driven mainly by the cloud top temperature and height, respectively, contribute most to the total CRE uncertainty.

Table 4-4: Relative uncertainties (in %) in COT and CRE retrievals as a total and separated by error source. The numbers reflect the median uncertainties from a full disk worth of SEVIRI retrievals (7 March 2017, 14:00 UTC). Pixels for which the observations were outside the look-up table or the visible surface albedo was larger than 0.6 were excluded. Results are shown separately for the 0.6–1.6 μm and the 0.6–3.8 μm retrievals as well as for liquid and ice clouds. Rows with a grey background contain the main error sources, some of which have been further separated as shown in the rows with a white background. The total uncertainty and the individual error source contributing most to the total uncertainty are indicated in bold face.

Error source	0.6–1.6 μm				0.6–3.8 μm			
	COT		CRE		COT		CRE	
	liquid	ice	liquid	ice	liquid	ice	liquid	ice
VIS reflectance	9.7	8.2	14.0	3.6	7.6	8.4	0.5	3.3
NIR reflectance	2.5	0.3	15.0	8.3	1.4	0.2	6.7	4.3
VIS+NIR reflectance	10.1	8.3	21.0	9.6	7.9	8.4	6.7	6.0
VIS surface albedo	2.4	1.1	3.9	0.6	1.5	1.0	0.1	0.5
NIR surface albedo	0.7	0.2	4.5	2.2	0.2	0.2	0.2	0.1
VIS+NIR surf. albedo	2.6	1.1	6.6	2.6	1.5	1.0	0.3	0.6
Absorption ozone	3.2	2.9	4.3	1.1	2.8	3.0	0.2	1.0
Absorption H_c	0.5	0.4	1.9	1.1	1.6	0.4	9.3	4.8
Absorption WVP	0.2	0.2	0.1	0.0	0.4	0.2	2.0	0.5
Absorption non-ozone	0.5	0.4	1.9	1.1	1.6	0.4	9.5	5.0
Emissivity T_s					0.3	0.2	1.3	1.7
Emissivity T_c					1.6	0.3	8.3	9.2
Emissivity total					1.8	0.3	9.9	13.8
Total	12.8	10.1	24.7	11.6	9.9	10.1	16.2	18.1

The numbers in Table 4-4 provide only a coarse indication of the uncertainty contributions. Results depend considerably on the surface type and atmospheric composition, and most importantly on the cloud properties themselves. The latter is illustrated in Figure 4-5 for the 0.6–1.6 μm retrieval. The relative COT uncertainty minimizes around COT=5, while it does not depend much on CRE. As noticed before, the main error source is the VIS reflectance. However, for thin clouds, surface albedo becomes an equally important error source. The relative CRE uncertainty decreases with COT, and reaches values over 50% for thin clouds. For most of the COT range, the CRE uncertainty is dominated by the NIR reflectance, while for thin clouds surface albedo (both VIS and NIR) becomes an even more important error source. Broadly, the relative CRE uncertainty also decreases with CRE. Figure 4-6 shows similar plots as Figure 4-5, but for the 0.6–3.8 μm channel combination. The results are comparable to each other in the case of COT, but for CRE the major contribution of in particular thermal emission to the uncertainty is evident. The difficulty to retrieve CRE for thin clouds is less severe when using the 3.8 μm channel, as is demonstrated by the much lower CRE

uncertainties in the small-COT range. However, toward large effective radii, the CRE uncertainty becomes very large and exceeds 50%. The reason is that the reflectance of clouds with larger ice particles becomes very low (see Figure 4-4), and lines of different CRE are almost on top of each other.

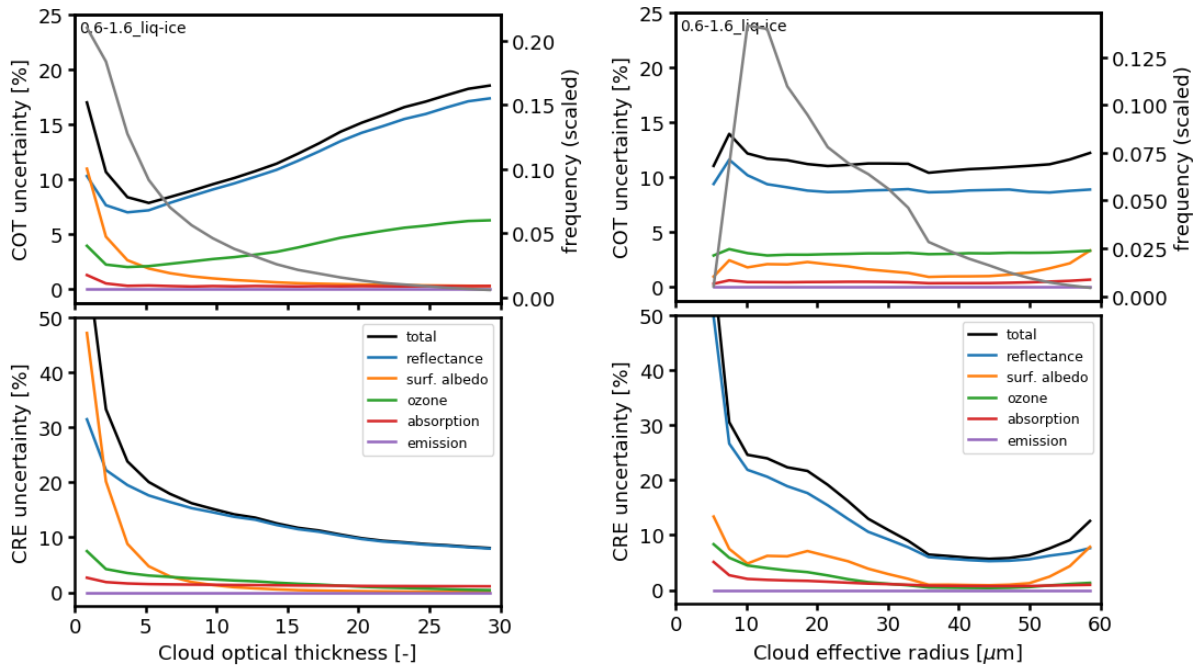


Figure 4-5: Dependence of COT and CRE uncertainties on COT and CRE of both liquid and ice clouds for the 0.6–1.6 μm retrieval. Uncertainties due to different error sources are shown separately. COT and CRE histograms are indicated by the grey lines.

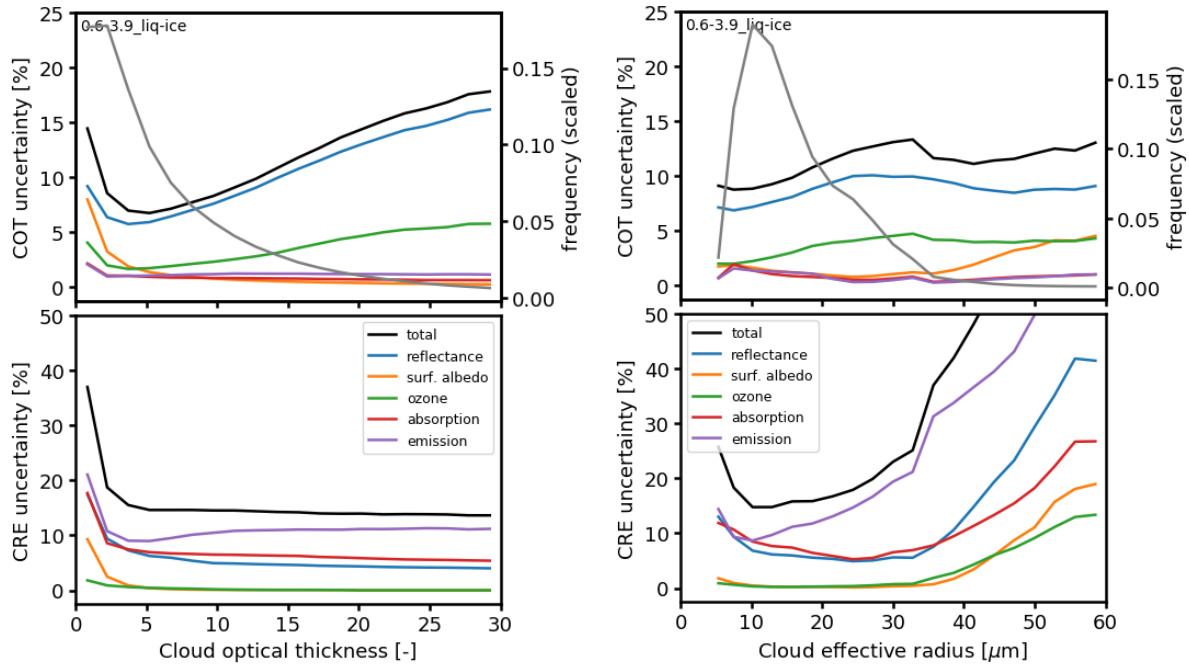


Figure 4-6: As Figure 4 5, but for the 0.6–3.8 μm retrieval.

Finally, the retrieval uncertainties are displayed against two ancillary parameters in Figure 4-7. This shows that the COT uncertainty increases considerably with solar zenith angle, while CRE shows a limited sensitivity. It should be noted that, since this analysis is based on SEVIRI observations, the solar zenith angle is correlated with the satellite zenith angle, so tendencies may also be related to that variable. The right panel in Figure 4-7 illustrates the enormous effect of the surface albedo: the COT uncertainty increases sharply for brighter surfaces and reaches the maximum reported value of 100% around a VIS surface albedo of 60%. The reason for these high uncertainties is that clouds can hardly be distinguished from such clear backgrounds.

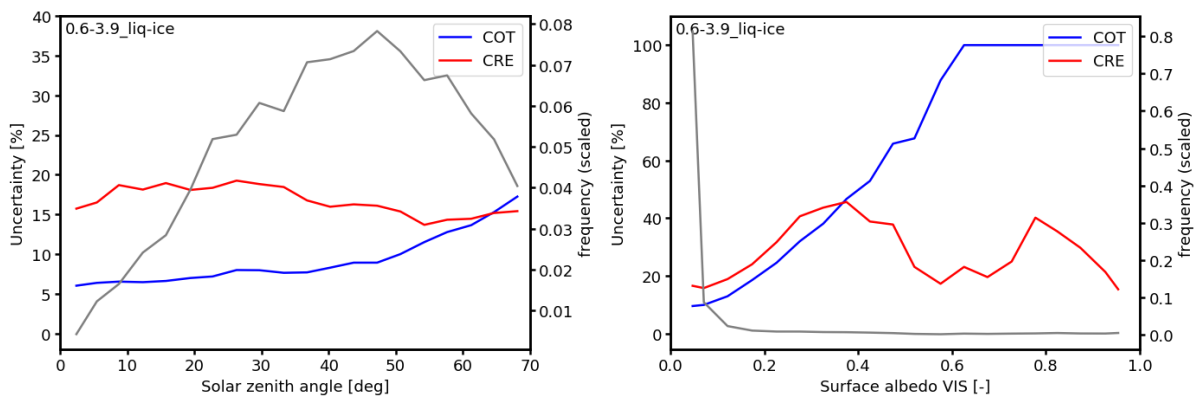


Figure 4-7: COT and CRE uncertainties as a function of solar zenith angle (left) and VIS surface albedo (right). COT and CRE histograms are indicated by the grey lines.

4.5 Practical Application

This section provides details on the SEVIRI instrument and other input data used by the CPP algorithm.

4.5.1 MSG-SEVIRI instrument

Meteosat Second Generation (Schmetz et al., 2002) is a series of European geostationary satellites that is operated by EUMETSAT. The first MSG satellite (Meteosat-8) was launched successfully in August 2002, and was followed by three more satellites (Meteosat-9, -10, and -11). MSG is a spinning stabilized satellite. The prime operational copy is positioned at an altitude of about 36,000 km above the equator and near 0° longitude. In full-disk mode, the SEVIRI instrument onboard MSG scans the complete disk of the Earth 4 times per hour, and operates 12 channels simultaneously.

An overview of the spectral characteristics of the SEVIRI channels is given in Table 4-5, while the shortwave channel spectral responses combined with a transmissivity spectrum are shown in Figure 4-8. Note that throughout this document channels are referred to by wavelengths rounded to one decimal. Thus, channel 1 is referred to as '0.6 μm', channel 2 as '0.8 μm', and channel 3 as '1.6 μm'. Channel 4 is referred to as '3.8 μm' for consistency with other imagers to which CPP is also applied and which have a slightly lower central wavelength than SEVIRI for the corresponding channel. The nominal spatial resolution of SEVIRI is 3x3 km². There is one channel measuring part of the earth disk at 1x1 km² sampling distance (called HRVIS), but this is not used by CPP.

Table 4-5: Overview of the SEVIRI channels operating at 3x3 km² spatial resolution. Channels used by CPP are indicated in bold.

Channel	Channel name	Central wavelength (μm)	Nominal spectral band (μm)
1	VIS006	0.635	0.56 - 0.71
2	VIS008	0.81	0.74 - 0.88
3	IR_016	1.64	1.50 - 1.78
4	IR_039	3.92	3.48 - 4.36
5	WV_062	6.25	5.35 - 7.15
6	WV_073	7.35	6.85 - 7.85
7	IR_087	8.70	8.30 - 9.10
8	IR_097	9.66	9.38 - 9.94
9	IR_108	10.80	9.80 - 11.80

10	IR_120	12.00	11.00 - 13.00
11	IR_134	13.40	12.40 - 14.40

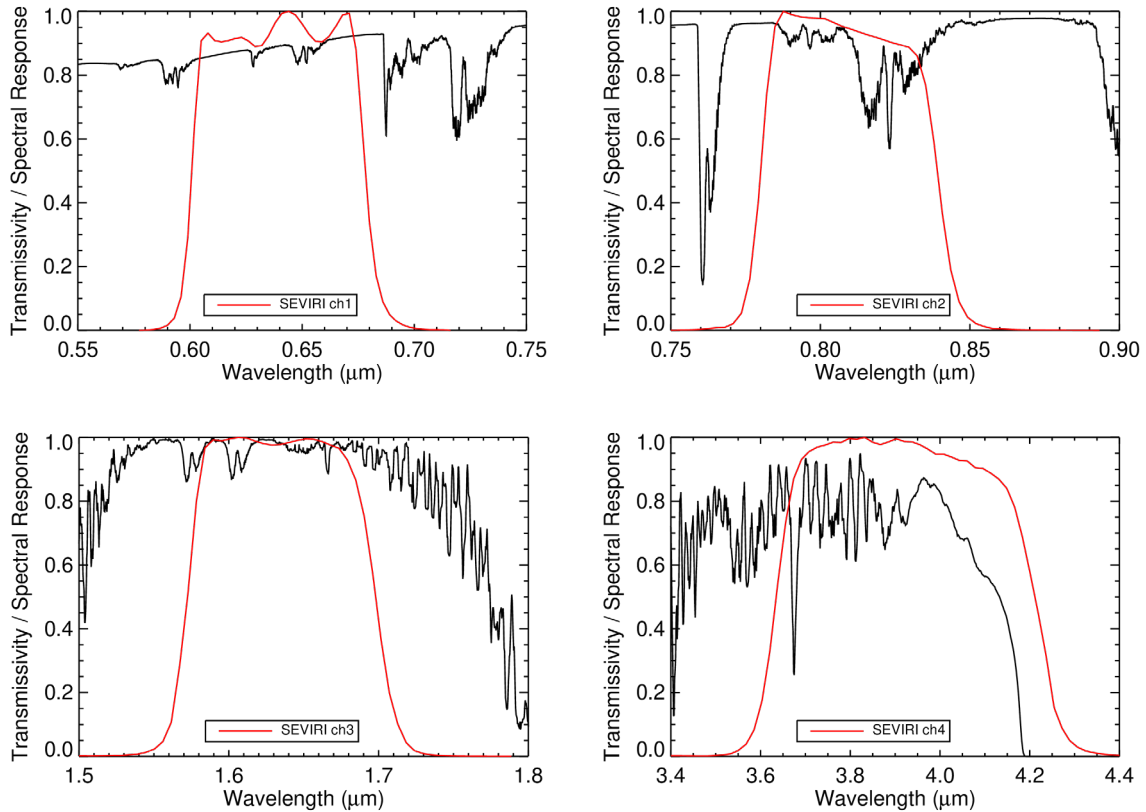


Figure 4-8: Spectral response functions (red) and transmissivity spectra in the corresponding wavelength ranges (black) for the SEVIRI shortwave channels 1 to 4. The (TOA to surface) transmissivity spectra were calculated with MODTRAN for a clear-sky MLS standard atmosphere at $\theta_0 = 45^\circ$.

4.5.2 Input data

In this section, the input data used to run the CPP algorithms are described.

Radiances

Radiances from the channels listed in Table 4-5 are the basic input.

Solar and satellite angles

The CPP algorithm requires the solar zenith angle θ_0 , the satellite viewing zenith angle θ , and the relative sun-satellite azimuth angle ϕ . These angles are calculated by the NWC SAF PPS software and passed on to CPP.

	Algorithm Theoretical Basis Document Cloud Physical Products SEVIRI	Doc. No: SAF/CM/KNMI/ATBD/SEVIRI/PP Issue: 3.3 Date: 08.08.2022
---	--	---

Cloud mask

A cloud mask is needed to decide for which pixels a cloud physical properties retrieval will be attempted. The probabilistic cloud mask of NWC SAF PPS is used for this purpose (see [RD 2] with additions in [RD 4]). Pixels with a cloud probability smaller than 50 % are labelled cloud-free, while pixels with a cloud probability equal to or larger than 50 % are labelled cloudy. CPP is applied to the latter.

Cloud-top height and temperature

CPP uses the CTTH product from NWC SAF PPS (see [RD 3] with additions in [RD 4]). The cloud top height is used for calculating the atmospheric correction and the cloud top temperature for estimating the contribution of thermal emission to the TOA radiance at 3.8 μm .

Surface albedo

The generation of surface albedo maps to be used for the CPP retrievals is outlined in the Appendix (Section 6).

Surface emissivity

For the 3.8- μm retrieval, a climatology compiled from four years of the MODIS-based surface emissivity database by Seemann et al. (2008) is used over land. Thus both the surface albedo and emissivity inputs are based on MODIS observations. Over snow-covered surfaces, ocean, and sea ice the surface emissivity is set to 1 minus the surface albedo estimated as described in the Appendix.

Numerical Weather Prediction (NWP) model fields

The following NWP model fields are required:

- Vertical profiles of temperature, pressure and humidity; 2-meter values of temperature, wind, and humidity; skin temperature; surface pressure. These are needed for the clear-sky and overcast radiance calculations.
- Water vapour path. For the atmospheric correction the water vapour path is needed.
- Sea ice. The concentration of sea ice is used to scale the surface albedo between values for water surfaces and typical values for sea ice (see Appendix).
- Snow depth and snow albedo. These properties are used only in the ICDR to correct the snow-free MODIS-based surface albedo for the presence of snow (see Appendix).

The NWP fields are obtained from ERA5 for the TCDR (Hersbach et al., 2020). For the ICDR, the preliminary ERA5 data stream, called ERA5T, is used.

Total ozone column

For the atmospheric correction the total ozone column is required. This is taken as a monthly mean climatology from the MSR dataset (Van der A et al., 2010).

4.5.3 Description of output

An overview of CPP output variables in the CLAAS-3 level-2 files is given in Table 4-6. All products except cph and cph_ext are available only in daylight conditions ($\theta_0 < 84^\circ$). The quantity h_σ (h_sigma) gives an indication of the homogeneity of the scene surrounding the pixel under consideration. It can help judging to what extent the retrieval assumption of horizontally homogeneous conditions is satisfied.

Table 4-6: CPP variables in level-2 files: name, description and units.

Name	Content	Units
cph	cloud-top thermodynamic phase, classes: liquid, ice; retrieval using 3.8- μ m channel	-
cph_ext	cloud-top thermodynamic phase, extended to more classes: water, super-cooled, opaque_ice, cirrus, overlap, overshooting_convection; retrieval using 3.8- μ m channel	-
cwp	cloud water path (LWP/IWP) ; retrieval using 3.8- μ m channel	kg m ⁻²
cot	cloud optical thickness; retrieval using 3.8- μ m channel	-
cre	cloud particle effective radius; retrieval using 3.8- μ m channel	m
cdnc	cloud droplet number concentration (only for liquid clouds) ; retrieval using 3.8- μ m channel	m ⁻³
cgt	cloud geometrical thickness (only for liquid clouds) ; retrieval using 3.8- μ m channel	m
cwp_unc	uncertainty estimate of cwp	kg m ⁻²
cot_unc	uncertainty estimate of cot	-
cre_unc	uncertainty estimate of cre	m
cdnc_unc	uncertainty estimate of cdnc	m ⁻³
cgt_unc	uncertainty estimate of cgt	m
processing_flag	status flag (bit flag) described in Table 4-7; retrieval using 3.8- μ m channel	-
h_sigma	ratio of standard deviation of $R_{0.6}$ to mean $R_{0.6}$ over 3x3 pixels	-
cph_16	as cph but using 1.6- μ m instead of 3.8- μ m channel	-
cph_16_ext	as cph_ext but using 1.6- μ m instead of 3.8- μ m channel	-
cwp_16	as cwp but using 1.6- μ m instead of 3.8- μ m channel	kg m ⁻²
cot_16	as cot but using 1.6- μ m instead of 3.8- μ m channel	-
cre_16	as cre but using 1.6- μ m instead of 3.8- μ m channel	m

cwp_16_unc	uncertainty estimate of cwp_16	kg m ⁻²
cot_16_unc	uncertainty estimate of cot_16	-
cre_16_unc	uncertainty estimate of cre_16	m
processing_flag_16	as processing_flag but using 1.6- μ m instead of 3.8- μ m channel	-

Table 4-7: CPP processing flag.

Bit number	Meaning
0	Sun-satellite angles ok for processing
1	NWP total column water vapour available
2	NWP surface temperature available
3	1.6- μ m channel used
4	3.8- μ m channel used
5	Input radiances ok for processing
6	Cloud-free retrieved by CPP
7	Phase changed by optical properties retrieval
8	VIS-NIR reflectance pair below solution space in LUT
9	VIS-NIR reflectance pair above solution space in LUT
10	Retrieval possibly affected by sunglint
11	High VIS surface albedo (> 60 %, typically due to snow cover / sea ice) according to auxiliary data
12	Negative NIR reflectance

5 Assumptions and Limitations

In this section some of the assumptions and limitations associated with the retrieval algorithms are listed.

- The derivation of cloud physical properties from reflected solar radiation is dependent on the availability of daylight. This means that no retrievals of cloud optical thickness, cloud particle effective radius and liquid/ice water path can be done during night time. For cloud phase an IR-based algorithm is used, which does operate during nighttime as well as daytime.
- Sun glint can affect the cloud property retrievals considerably, in particular for broken cloudy scenes over ocean. Therefore, possibly sun glint-affected pixels (defined by a scattering angle differing less than 27 degrees from the direct glint angle) are flagged.
- Cloud retrievals are performed assuming that clouds are plane parallel. This is true only in a minority of cases, which implies that retrieval errors become larger as clouds deviate from being plane parallel. Especially convective clouds can be problematic, as they frequently have illuminated and shadowed sides (see, e.g., Marshak et al. 2006). Broken and sub-pixel cloud fields, including cloud edges, can also cause problems for retrieving cloud properties, since a passive satellite sensor measures an averaged radiance of the cloudy and cloud-free part of a pixel. The error made in these cases is among others dependent on the contrast between clouds and underlying surface, the true properties of the cloud, and the cloud fraction within the sampling resolution of the instrument (Oreopoulos and Davies 1998; Coakley et al. 2005; Wolters et al. 2010).
- The retrieval is highly problematic over very bright surfaces, particularly ice and snow, as the visible reflectance from clouds is similar to that from the surface.
- Unlike active satellite instruments, which can derive cloud profile information, retrievals from passive satellite instruments are limited by the fact that the obtained signal emanates from the integrated profile. Since near-infrared radiation is only penetrating into the cloud to a certain depth (due to absorption by cloud particles), the retrieved cloud phase and cloud particle effective radius are representative for the upper part of the cloud (Platnick, 2001). The penetration depth depends on the amount of absorption by cloud particles, which overall increases with wavelength. This means that the retrieved CPH and r_e depend on which NIR spectral channel is used (in our case 1.6 or 3.8 μm). See, for example, Rosenfeld et al. (2004) for a discussion on pros and cons of the use of different NIR channels. Seethala and Horvath (2010) and Zhang and Platnick (2011) noted that the 3.8 μm r_e can be significantly smaller than the 1.6 μm r_e in non-raining stratocumulus (Sc) clouds, for which one would expect, in contrast, an increase in r_e from 1.6 to 3.8 μm . They suggested that drizzle and/or 3D inhomogeneity effects might be the cause. Zhang et al. (2012) further investigated the effects of drizzle and cloud horizontal inhomogeneity on MODIS r_e retrievals using Large Eddy Simulation (LES) models and synthetic retrievals and found that drizzle does not have a strong impact but inhomogeneity, the plane-parallel bias, does.
- In the derivation of equations (3) for LWP and (7) for IWP it is assumed that the cloud particle effective radius is vertically uniform. On the other hand, the ISBLC model used to derive CDNC and CGT, yields an increasing effective radius with height. While stratocumulus clouds normally obey (sub-)adiabatic theory, leading to vertical profiles

as in the ISBLC model, this is typically not the case for cumulus clouds, which tend to have a more uniform vertical profile (see Grosvenor et al., 2018 and references therein). Deviations from vertical homogeneity are also common for ice clouds. Thick ice clouds often have small ice crystals at the top, which are not representative of the full vertical extent. As a consequence, IWP can be underestimated in these cases. Results are even more questionable for multi-layer cloud systems. Here the derived effective radius (uppermost cloud) may be totally unrelated to any cloud below, so the relation between r_e and LWP/IWP is not applicable here.

- Aerosols are not considered in the CPP retrieval. This assumption is usually justified because aerosols reside below or within the cloud and their optical thickness is small compared to that of the cloud. However, if the aerosols reside above the cloud and if they are sufficiently absorbing, they can significantly lower the visible reflectance. The effect on the retrievals depends on the channel combination used and on the aerosol properties (Haywood et al. 2004). The impact is strongest for the 1.6- μm channel, with a possible underestimation of r_e by several micrometers. For the 3.8- μm channel, the impact is smaller and can be an overestimation of r_e . Cloud optical thickness generally has a low bias. Although the annual mean effect of absorbing aerosols is relatively small, their instantaneous effect on LWP can be as high as a 40 g m⁻² low bias, mostly caused by a reduction in optical thickness. Seethala et al. (2018) analysed absorbing aerosol effects on CLAAS-2 SEVIRI and MODIS LWP by comparing them with passive microwave retrievals and quantifying the aerosol load with the help of Ozone Monitoring Instrument (OMI) aerosol index.
- Precipitation may have an effect on cloud property retrievals in case the radiation penetrates sufficiently deep into the cloud to be affected by the (large) precipitating droplets. Retrievals with the 1.6- μm channel are expected to be most sensitive to this, but synthetic studies (e.g., Zinner et al. 2010; Zhang et al. 2012) have not indicated significant impact on the effective radius retrieval.
- Many assumptions are made for the calculation of LUTs with DAK. These include: the absence of aerosols, the location of liquid clouds between 1 and 2 km height and of ice clouds between 5 and 6 km height, the specific habits and resulting phase functions of ice crystals, and the type and width of water droplet effective radius distributions. The necessity of these assumptions is an illustration of the heavily underconstrained nature of the cloud physical properties retrieval principle.

	<p style="text-align: center;">Algorithm Theoretical Basis Document Cloud Physical Products SEVIRI</p>	<p>Doc. No: SAF/CM/KNMI/ATBD/SEVIRI/ CPP Issue: 3.3 Date: 08.08.2022</p>
---	---	--

6 Appendix

A spatially complete (gap-filled) land surface albedo dataset, in both the VIS and NIR spectral bands used in the CPP, is required for the cloud retrievals. Due to the different nature of the TCDR and ICDR processing, different procedures are used to generate corresponding surface albedo maps.

6.1 Surface albedo for TCDR

A surface albedo dataset was created based on the MODIS Collection 6 level 3 white-sky albedo dataset (MCD43C3). These data are available globally on a daily basis and on a regular, $0.05^\circ \times 0.05^\circ$ latitude-longitude grid, and span the complete MODIS period. Here, data from the period 2003-2020 were used, which are based on both Terra and Aqua full-year retrievals, and cover sufficiently also the MSG-SEVIRI period.

The creation of the gap-filled albedo dataset was based on a combination of a gap-filled intra-annual climatology and the time series of the original daily albedo data. The gap-filled climatology is also daily (365 days). It is computed on a pixel basis by averaging albedo values of corresponding days in the 18-year time series. Only retrievals with MODIS QA index lower (better) or equal to 3 (25% or less fill values during inversion) are allowed in this step. The remaining gaps are filled using linear interpolation, and the resulting 365 values per pixel are further smoothed using a running weighted-average approach: a 9-day running interval is used, centered on each day. The average is weighted with the number of years (n_{years}) used for the calculation of each day's climatology (maximum 18 years) plus one. Hence, the interpolated values have weight 1, and the existing values have weight $n_{\text{years}}+1$. After this process, 99.83% of land type pixels are filled with albedo values. The few remaining empty pixels are filled by spatial averaging of nearby values, using successively averaging windows of 3×3 , 5×5 etc. pixels, until a value is computed.

The final, gap-filled 18-year long daily time series is computed as a linear combination of the original MODIS time series and the gap-filled daily climatology. For the original time series the same quality flags, as in the calculation of the climatology described before, apply. Following the approach of Greuell et al. (2013), the final gap-filled time series C_i is computed from $C_i = w_A A_i + (1 - w_A) B_i$, where A_i is the initial time series with no-data days filled with linear interpolation, B_i is the daily climatology and $w_A = \text{MAX}(1 - \Delta i/80; 0)$, where Δi is the distance (in days) of day i from the closest day with valid value from the original time series. Hence, in the extreme case where a day is in the middle of a 160-days-with-no-data interval (or larger), it acquires a purely climatological value. Three quality flags associated with the final gap-filled time series calculations are also saved: the initial MODIS QA flag, the "day-distance" Δi and n_{years} , the number of years used in the calculation of the climatology.

The surface albedo time series created in this way includes values for all land surfaces, i.e. including when they are snow-covered. No further information on snow cover (e.g., from NWP) is therefore used.

For the white-sky surface albedo over ocean, constant values are prescribed based on Jin et al. (2011). These values, 4.8%, 4.4%, and 4.9%, for the 0.6-, 1.6-, and 3.8- μm channels,

	<p style="text-align: center;">Algorithm Theoretical Basis Document Cloud Physical Products SEVIRI</p>	<p>Doc. No: SAF/CM/KNMI/ATBD/SEVIRI/CP Issue: 3.3 Date: 08.08.2022</p>
---	---	--

respectively, were calculated for a wind speed of 10 m s^{-1} . Variations with wind speed are less than 0.4% up to 15 m s^{-1} . At higher wind speeds, whitecap foam causes a somewhat larger increase in albedo, but this is neglected here.

The concentration of sea ice from ERA5 is used to correct the albedo of ocean for the presence of ice. The correction for sea ice is implemented as follows: $\alpha_{\text{s}} = \alpha_{\text{s,ice}} f_{\text{ice}} + \alpha_{\text{s,water}} [(1-f_{\text{ice}})]$, where f_{ice} is the sea ice concentration and $\alpha_{\text{s,ice}}$ is the channel-dependent, prescribed sea-ice albedo. The latter is set to 90%, 13%, and 1.3%, for the 0.6-, 1.6-, and 3.8- μm channels, respectively, as estimated from MODIS white-sky surface albedo/emissivity maps over sea ice regions.

6.2 Surface albedo for ICDR

A surface albedo climatology was created based on the gap-filled snow-free MODIS Collection 6 level 3 white-sky albedo dataset (MCD43GF) for the required channels (Sun et al. 2017). These data are available globally on a daily basis and on a $\sim 1000 \text{ m}$ latitude-longitude grid, and span the period 2000-2017. Here, data from the period 2003-2017 were used, which are based on both Terra and Aqua full-year retrievals. The climatology was computed on a daily basis and on a $0.05^\circ \times 0.05^\circ$ latitude-longitude grid. To this end, the original MCD43GF albedo data were averaged on a 6×6 grid cells basis, to match the desired resolution. Corresponding quality indices (0-7, 0 being the best quality) were also averaged, and the reciprocal of their average was used as weight of the resulting 0.05° grid cell albedo in the temporal averaging (to avoid divisions by zero, the value 1 was first added to all quality indices; thus, best quality values have weight 1, and worst quality values have weight 0.125). The climatological value for a grid cell and a specific day in the year was then computed as the weighted average of values from the 15 available years. Over coastal areas, an additional step was taken: after calculating the land albedo as before, the 0.05° grid cell albedo was calculated as $\alpha_{\text{s}} = \alpha_{\text{s,land}} f_{\text{land}} + \alpha_{\text{s,ocean}} (1 - f_{\text{land}})$, where f_{land} , the fraction of land, was calculated as the fraction of $6 \times 6 = 36$ MCD43GF grid cells available.

In addition to the snow-free albedo climatology, snow depth and snow albedo from ERA5T are used to correct the MODIS albedo in case of snow on the ground. The snow depth d_{snow} , in meters of water equivalent, is converted to a snow cover fraction f_{snow} according to $f_{\text{snow}} = \text{MIN}(d_{\text{snow}}/0.1, 1)$, which is a simplified form of relations used in the ECMWF IFS model. The snow cover fraction is then used as a weight between the snow albedo, $\alpha_{\text{s,snow}}$, and the snow-free MODIS surface albedo: i.e. $\alpha_{\text{s}} = \alpha_{\text{s,snow}} f_{\text{snow}} + \alpha_{\text{s,MODIS}} (1 - f_{\text{snow}})$. The snow albedo at 0.6 μm is determined by multiplying the ERA5T broad-band value by 1.12, based on comparisons between ERA5-modelled broad-band and MODIS-observed 0.6 μm surface albedo over snow surfaces (mainly Greenland and Antarctica), while the snow albedo at 1.6 and 3.8 μm is set to fixed values of 13% and 1.3%, respectively, as estimated from MODIS white-sky surface albedo/emissivity maps over snow regions.

The albedo over ocean is specified exactly the same as for the TCDR. Note, however, that a number of shallow near-coastal water regions have a valid albedo from the TCDR approach, while in the ICDR their albedo is set to the fixed values used over ocean. The treatment of sea ice is also the same as for the TCDR, albeit with different sea ice concentration data.

7 References

Anderson, G. P., S. A. Clough, F. X. Kneizys, J. H. Chetwynd, and E. P. Shettle, 1986: AFGL Atmospheric Constituent Profiles (0-120km). Tech. Rep. AFGL-TR-86-0110, 43 pp.

Baum, B. A., P. Yang, A. J. Heymsfield, C. G. Schmitt, Y. Xie, A. Bansemer, Y.-X. Hu, and Z. Zhang, 2011: Improvements in shortwave bulk scattering and absorption models for the remote sensing of ice clouds, *J. Appl. Meteorol. Clim.*, 50, 1037-1056, doi:10.1175/2010JAMC2608.1.

Baum, B. A., 2014: Ice cloud bulk scattering models, https://www.ssec.wisc.edu/ice_models/.

Benas, N., S. Finkensieper, M. Stengel, G.-J. van Zadelhoff, T. Hanschmann, R. Hollmann, and J. F. Meirink, 2017: The MSG-SEVIRI-based cloud property data record CLAAS-2, *Earth System Science Data*, 9, 415–434, doi:10.5194/essd-9-415-2017.

Benas, N., J. F. Meirink, M. Stengel, and P. Stammes, 2019: Sensitivity of liquid cloud optical thickness and effective radius retrievals to cloud bow and glory conditions using two SEVIRI imagers, *Atmos. Meas. Tech.*, 12, 2863-2879, doi: 10.5194/amt-12-2863-2019.

Bennartz, R. and J. Rausch, 2017: Global and regional estimates of warm cloud droplet number concentration based on 13 years of AQUA-MODIS observations, *Atmos. Chem. Phys.*, 17, 9815-9836, doi:10.5194/acp-17-9815-2017.

Berk, A., G. P. Anderson, P. K. Acharya, J. H. Chetwynd, L.S. Bernstein, E. P. Shettle, M. W. Matthew, and S. M. Adler-Golden, 2000: MODTRAN4 Version 2 Users Manual. Technical report, Air Force Materiel Command, Air Force Research Laboratory, Space Vehicles Directorate, Hanscom AFB, MA 01731, USA.

Borg, L. A. and R. Bennartz, 2007: Vertical structure of stratiform marine boundary layer clouds and its impact on cloud albedo, *Geophys. Res. Lett.*, 34, L05807, doi:10.1029/2006GL028713.

Caudill, T. R., D. E. Flittner, B. M. Herman, O. Torres, and R. D. McPeters, 1997: Evaluation of the pseudo-spherical approximation for backscattered ultraviolet radiances and ozone retrieval, *J. Geophys. Res.*, 102, D3, 3881-3890.

Chandrasekhar S., 1960: Radiative Transfer, New York, Dover, 393 pp.

Coakley, J. A., M. A. Friedman, and W. R. Tahnk, 2005: Retrieval of cloud properties for partly cloudy imager pixels, *J. Atmos. Ocean. Technol.*, 22, 3–17.

De Haan, J. F., P. Bosma, and J. W. Hovenier, 1987: The adding method for multiple scattering calculations of polarized light, *Astron. Astrophys.*, 183, 371-391.

Evans, K. F., 1998: The Spherical Harmonics Discrete Ordinate, Method for Three-Dimensional Atmospheric Radiative Transfer. *J. Atmos. Sci.*, 55, 429-446.

Greuell, W., J. F. Meirink, and P. Wang, 2013: Retrieval and validation of global, direct, and diffuse irradiance derived from SEVIRI satellite observations, *Journal of Geophysical Research: Atmospheres*, 118, 2340–2361, doi:10.1002/jgrd.50194.

Grosvenor, D. P., O. Souderval, P. Zuidema, A. S. Ackerman, M. D. Alexandrov, R. Bennartz, R. Boers, B. Cairns, J. C. Chiu, M. Christensen, H. Deneke, M. Diamond, G. Feingold, A. Fridlind, A. Hünerbein, C. Knist, P. Kollias, A. Marshak, D. McCoy, D. Merk, D. Painemal, J. Rausch, D. Rosenfeld, H. Russchenberg, P. Seifert, K. Sinclair, P. Stier, B. van Diedenhoven, M. Wendisch, F. Werner, R. Wood, Z. Zhang, and J. Quaas, 2018: Remote sensing of cloud droplet number concentration: Review of current and perspectives for new approaches. *Rev. Geophys.*, 56, no. 2, 409-453, doi:10.1029/2017RG000593.

Håkansson, N., C. Adok, A. Thoss, R. Scheirer, and S. Hörnquist, 2018: Neural network cloud top pressure and height for MODIS, *Atmos. Meas. Tech.*, 11, 3177–3196, <https://doi.org/10.5194/amt-11-3177-2018>.

Hansen, J. (1971): Multiple scattering of polarized light in planetary atmospheres. Part II. Sunlight reflected by terrestrial water clouds, *J. Atmos. Sci.*, 28, 1400–1426.

Haywood, J.M., S.R. Osborne, and S.J. Abel, 2004: The effect of overlying absorbing aerosol layers on remote sensing retrievals of cloud effective radius and cloud optical depth, *Quart. J. Roy. Meteorol. Soc.*, 130, 779-800, doi: 10.1256/qj.03.100.

Heidinger A.K. and M.J. Pavolonis, 2009: Gazing at cirrus clouds for 25 years through a split window. Part I: Methodology, *J. Appl. Meteorol. Clim.*, 48, 1100-1116, doi: 10.1175/2008JAMC1882.1.

Hersbach, H., B. Bell, P. Berrisford, S. Hirahara, A. Horányi, J. Muñoz-Sabater, J. Nicolas, C. Peubey, R. Radu, D. Schepers, A. Simmons, C. Soci, et al., 2020: The ERA5 global reanalysis, *Quart. J. Roy. Meteorol. Soc.*, 146, 1999-2049, doi: 10.1002/qj.3803.

Hess, H, R. B. A. Koelemeijer, and P. Stammes, 1998: Scattering matrices of imperfect hexagonal crystals. *J. Quant. Spectrosc. Radiat. Transfer*, 60, 301–308.

Jin, Z., Y. Qiao, Y. Wang, Y. Fang, and W. Yi, 2011: A new parameterization of spectral and broadband ocean surface albedo, *Opt. Express*, 19, 26429–26443, doi:10.1364/OE.19.026429.

Karlsson, K.-G., K. Anttila, J. Trentmann, M. Stengel, J. F. Meirink, A. Devasthale, T. Hanschmann, S. Kothe, E. Jaaskelainen, J. Sedlar, N. Benas, G.-J. van Zadelhoff, C. Schlundt, D. Stein, S. Finkensieper, N. Håkansson, and R. Hollmann, 2017: CLARA-A2: the second edition of the CM^oSAF cloud and radiation data record from 34 years of global AVHRR data, *Atmospheric Chemistry and Physics*, 17, 5809-5828, doi:10.5194/acp-17-5809-2017.

Macke, A., D. Mitchell, and L. von Bremen, 1999: Monte Carlo radiative transfer calculations for inhomogeneous mixed phase clouds. *Phys. Chem. Earth*, 24-3, 237-241.

Marshak, A., S. Platnick, T. Várnai, G. Wen, and R. F. Cahalan, 2006: Impact of three-dimensional radiative effects on satellite retrievals of cloud droplet sizes, *J. Geophys. Res.*, 111, 9207–9218.

Meirink, J.F., R. A. Roebeling, and P. Stammes, 2009: Atmospheric correction for the KNMI Cloud Physical Properties retrieval algorithm, KNMI publication: TR-304, 17/2/2009, pp22.

Meirink, J. F., R. A. Roebeling, and P. Stammes, 2013: Inter-calibration of polar imager solar channels using SEVIRI, *Atm. Meas. Tech.*, 6, 2495-2508, doi:10.5194/amt-6-2495-2013.

Nakajima, T., and M. D. King, 1990: Determination of the Optical Thickness and Effective Particle Radius of Clouds from Reflected Solar Radiation Measurements. Part 1: Theory. *J. Atmos. Sci.*, 47, 1878-1893.

Nakajima, T. Y., and T. Nakajima, 1995: Wide-Area Determination of Cloud Microphysical Properties from NOAA AVHRR Measurements for FIRE and ASTEX regions. *J. Atmos. Sci.*, 52, 4043 – 4059.

Oreopoulos, L., and R. Davies, 1998: Plane parallel albedo biases from satellite observations. part I: Dependence on resolution and other factors: *J. Climate*, 11 , 919–932.

Pavolonis, M. J., A. K. Heidinger, and T. Uttal, 2005: Daytime global cloud typing from AVHRR and VIIRS: Algorithm description, validation, and comparison, *J. Appl. Meteorol.*, 44, 804-826.

Platnick, S., 2001: A superposition technique for deriving mean photon scattering statistics in plane-parallel cloudy atmospheres, *J. Quant. Spectrosc. Radiat. Transfer*, 68, 57-73

Platnick, S., K. G. Meyer, M. D. King, G. Wind, N. Amarasinghe, B. Marchant, G. T. Arnold, Z. Zhang, P. A. Hubanks, R. E. Holz, P. Yang, W. L. Ridgway, and J. Riedi, 2017: The MODIS Cloud Optical and Microphysical Products: Collection 6 Updates and Examples From Terra and Aqua, *IEEE T. Geosci. Remote*, 55, 502–525, doi: 10.1109/TGRS.2016.2610522.

Rodgers, C. D., 2000: Inverse methods for atmospheric sounding: theory and practice, World Scientific, Hackensack, NJ, USA, 238 pp.

Roebeling, R. A., 2008: Cloud Physical Properties Retrieval for Climate Studies using SEVIRI and AVHRR data, PhD Thesis, Wageningen University, The Netherlands, 160pp. Available from <http://www.knmi.nl/publications>.

Roebeling, R. A., A. Berk, A. J. Feijt, W. Frerichs, D. Jolivet, A. Macke, and P. Stammes, 2005: Sensitivity of cloud property retrievals to differences in narrow band radiative transfer simulations, KNMI Scientific Report, WR 2005-02, Royal Netherlands Meteorological Institute, De Bilt, the Netherlands, 27 pp. Available from <http://www.knmi.nl/publications>.

Roebeling, R. A., A. J. Feijt, and P. Stammes, 2006: Cloud property retrievals for climate monitoring: implications of differences between SEVIRI on METEOSAT-8 and AVHRR on NOAA-17, *J. Geophys. Res.*, 111, D20210, doi:10.1029/2005JD006990.

Schmetz, J., P. Pili, P., S. Tjemkes, D. Just, J. Kerkmann, S. Rota, and A. Ratier, 2002: An Introduction to Meteosat Second Generation, *Bull. Amer. Meteorol. Soc.*, 83, 7, 977-992.

Schumann, U., B. Mayer, K. Gierens, S. Unterstrasser, P. Jessberger, A. Petzold, C. Voigt, J.-F. Gayet, 2011: Effective radius of ice particles in cirrus and contrails. *J. Atmos. Sci.*, 68, 300–321, doi:10.1175/2010JAS3562.1.

Seemann, S.W., E. E. Borbas, R. O. Knuteson, G. R. Stephenson, H.-L. Huang, 2008: Development of a Global Infrared Land Surface Emissivity Database for Application to Clear

	Algorithm Theoretical Basis Document Cloud Physical Products SEVIRI	Doc. No: SAF/CM/KNMI/ATBD/SEVIRI/CP Issue: 3.3 Date: 08.08.2022
---	--	---

Sky Sounding Retrievals from Multi-spectral Satellite Radiance Measurements, *J. Appl. Meteorol. Clim.*, 47, 108-123.

Seethala, C. and A. Horvath, 2010: Global assessment of AMSR-E and MODIS cloud liquid water path retrievals in warm oceanic clouds, *J. Geophys. Res.*, 115, D13202, doi:10.1029/2009JD012662.

Seethala, C., J. F. Meirink, A. Horvath, R. Bennartz, and R. Roebeling, 2018: Evaluating the diurnal cycle of South Atlantic stratocumulus clouds as observed by MSG SEVIRI, *Atmospheric Chemistry and Physics*, 18, 13 283–13 304, doi:10.5194/acp-18-13283-2018.

Segelstein, D., 1981: The complex refractive index of water, M.Sc. Thesis, Univ. of Missouri, Kansas City.

Stammes, P., 2001: Spectral radiance modeling in the UV-Visible range. *IRS 2000: Current problems in Atmospheric Radiation*, edited by W.L. Smith and Y.M. Timofeyev, pp 385-388, A. Deepak Publ., Hampton, Va.

Stamnes, K., S. C Tsay, W. Wiscombe, and K Jayaweera, 1988: Numerically stable algorithm for discrete ordinate method radiative transfer in multiple scattering and emitting layered media. *Appl. Optics*, 27, 2502-2509.

Stengel, M., A. Kniffka, J. F. Meirink, M. Lockhoff, J. Tan, and R. Hollmann, 2014: CLAAS: the CM SAF cloud property data set using SEVIRI, *Atmos. Chem. Phys.*, 14, 4297–4311, doi:10.5194/acp-14-4297-2014.

Stephens, G. L., 1978: Radiation profiles in extended water clouds: II. Parameterization schemes. *J. Atmos. Sci.*, 35, 2123-2132.

Stephens, G. L. and C. D. Kummerow, 2007: *The Remote Sensing of Clouds and Precipitation from Space: A Review*. *J. Atmos. Sci.*, 64 , 3742–3765.

Sun, Q., Wang, Z., Li, Z., Erb, A., and Schaaf, C. L. B., 2017: Evaluation of the global MODIS 30 arc-second spatially and temporally complete snow-free land surface albedo and reflectance anisotropy dataset. *Int. J. Appl. Earth Obs.*, 58, 36-49, doi: 10.1016/j.jag.2017.01.011.

Van der A, R. J., Allaart, M. A. F., and Eskes, H. J., 2010: Multi sensor reanalysis of total ozone, *Atmos. Chem. Phys.*, 10, 11277–11294, doi:10.5194/acp-10-11277-2010.

Warren, S. G. and R. E. Brandt, 2008: Optical constants of ice from the ultraviolet to the microwave: A revised compilation. *J. Geophys. Res.*, 113, D14220, doi:10.1029/2007JD009744.

Watts, P. D., C. T. Mutlow, A. J. Baran, and A. M. Zavody, 1998: *Study on Cloud Properties derived from Meteosat Second Generation Observations, Final Report*, EUMETSAT ITT no. 97/181.

Wolters, E. L. A., H. M. Deneke, B. J. J. M. van den Hurk, J. F. Meirink, and R. A. Roebeling, 2010: Broken and inhomogeneous cloud impact on satellite cloud particle effective radius and cloud-phase retrievals, *J. Geophys. Res.*, 115, doi:10.1029/2009JD012205.

	Algorithm Theoretical Basis Document Cloud Physical Products SEVIRI	Doc. No: SAF/CM/KNMI/ATBD/SEVIRI/ CPP Issue: 3.3 Date: 08.08.2022
---	--	---

Wolters, E. L. A., R. A. Roebeling, and P. Stammes, 2006: Cloud reflectance calculations using DAK: study on required integration points, KNMI Technical Report, TR-292, Royal Netherlands Meteorological Institute, De Bilt, The Netherlands, 17 pp. Available from <http://www.knmi.nl/publications>.

Yang, P., L. Bi, B. A. Baum, K.-N. Liou, G. W. Kattawar, M. I. Mishchenko, and B. Cole, 2013: Spectrally consistent scattering, absorption, and polarization properties of atmospheric ice crystals at wavelengths from 0.2 to 100 μm , *J. Atmos. Sci.*, 70, 330-347, doi:10.1175/JAS-D-12-039.1.

Zhang, Z., A. S. Ackerman, G. Feingold, S. Platnick, R. Pincus, and H. Xue, 2012: Effects of cloud horizontal inhomogeneity and drizzle on remote sensing of cloud droplet effective radius: Case studies based on large-eddy simulations, *J. Geophys. Res.*, 117, D19208, doi:10.1029/2012JD017655.

Zhang, Z., and S. Platnick, 2011: An assessment of differences between cloud effective particle radius retrievals for marine water clouds from three MODIS spectral bands, *J. Geophys. Res.*, 116, D20215, doi:10.1029/2011JD016216.

Zhang, Z., P. Yang, G. Kattawar, Riedi, J., Labonnote, L. C., Baum, B. A., Platnick, S., and Huang, H.-L., 2009: Influence of ice particle model on satellite ice cloud retrieval: lessons learned from MODIS and POLDER cloud product comparison, *Atmos. Chem. Phys.*, 9, 7115-7129, doi: 10.5194/acp-9-7115-2009.

Zinner, T., G. Wind, S. Platnick, and A. S. Ackerman, 2010: Testing remote sensing on artificial observations: impact of drizzle and 3-D cloud structure on effective radius retrievals, *Atmos. Chem. Phys.*, 10, 9535-9549, doi:10.5194/acp-10-9535-2010.

8 Glossary

Acronyms and other terms occurring in this document are explained in Table 8-1 and Table 8-2, respectively.

Table 8-1: Explanation of abbreviations and acronyms included in this document.

Acronym / abbreviation	Definition
AMF	Air Mass Factor
ATBD	Algorithm Theoretical Basis Document
AVHRR	Advanced Very High Resolution Radiometer
BT	Brightness Temperature
CDNC	Cloud Droplet Number Concentration
CDO	Climate Data Operators
CGT	Cloud Geometrical Thickness
CLAAS	Cloud property dataset using SEVIRI
CLARA-A	Cloud, Albedo And Surface Radiation dataset from AVHRR data
CLAVR-x	Clouds from AVHRR Extended
CM ^o SAF	Climate Monitoring SAF
COT (or τ)	Cloud Optical Thickness
CPH	Cloud thermodynamic Phase
CPP	Cloud Physical Properties
CRE (or r_e)	Cloud particle Effective Radius
CTH	Cloud Top Height
CTT	Cloud Top Temperature
CWP	Cloud Water Path
DAK	Doubling Adding KNMI
DISORT	Discrete Ordinates
DWD	Deutscher Wetterdienst (German Met Service)
ECMWF	European Centre for Medium-Range Weather Forecasts
EUMETSAT	European Organisation for the Exploitation of Meteorological Satellites
ICDR	Interim Climate Data Record
IR	Infrared (wavelength range)
ISBLC	Idealized Stratiform Boundary Layer Cloud
IWC	Ice Water Content
IWP	Ice Water Path

KNMI	Koninklijk Nederlands Meteorologisch Instituut (Dutch Met Service)
LES	Large Eddy Simulation
LUT	Look-Up Table
LWC	Liquid Water Content
LWP	Liquid Water Path
MLS	Mid-Latitude Summer
MODIS	Moderate Resolution Imaging Spectroradiometer
MODTRAN	MODerate spectral resolution atmospheric TRANsmittance and radiance code
MSG	Meteosat Second Generation
NIR	Near-Infrared (wavelength range)
NOAA	National Oceanic and Atmospheric Administration
NWC SAF	Nowcasting and Very Short Range Forecasting SAF
NWP	Numerical Weather Prediction
OMI	Ozone Monitoring Instrument
OSI SAF	Ocean and Sea Ice SAF
RTM	Radiative Transfer Model
RTTOV	Radiative Transfer for TOVS
SAF	Satellite Application Facility
Sc	Stratocumulus
SEVIRI	Spinning Enhanced Visible and Infrared Imager
SHDOM	Spherical Harmonics Discrete Ordinates Method
SMHI	Swedish Meteorological and Hydrological Institute
TCDR	Thematic Climate Data Record
TCO	Total Column Ozone
TOA	Top Of Atmosphere
UV	Ultraviolet (wavelength range)
VIS	Visible (wavelength range)
WVP	Water Vapour Path

Table 8-2: Explanation of terms used in this document.

Term	Meaning
Brightness temperature	The temperature of a blackbody producing the same radiative flux as the observed flux in a given spectral band.
Cloud cover	Fraction of the sky obscured by clouds.

Cloud droplet number concentration	Amount of cloud droplets per volume unit, here assumed to be constant with height in the cloud (ISBLC model)
Cloud geometrical thickness	Vertical distance between the bottom and the top of the cloud
Cloud mask	Index specifying whether a satellite observed pixel is clear or cloudy, with possible additional categories such as 'cloud-contaminated'.
Cloud optical thickness	The optical thickness due to clouds. It is defined here at 0.6 μm with reference to a vertical path through the atmosphere.
Cloud-top height	Height above the surface of the upper boundary of a cloud.
Cloud-top temperature	Temperature at the upper boundary of a cloud.
Cloud water path	The total mass of cloud particles in a vertical column.
Effective radius	The ratio of the volume of (cloud) particles to their projected surface area.
Ice water path	The total mass of cloud ice particles in a vertical column.
Liquid water path	The total mass of cloud liquid particles (droplets) in a vertical column.
Optical thickness	Also: optical depth. The negative natural logarithm of the fraction of radiation at a particular wavelength that is not scattered or absorbed on a path.
Reflectance	The ratio of reflected radiation in a certain direction to incident radiation. It can relate to a particular wavelength as well as to a spectral band.
Surface albedo	The reflectance of a surface integrated over all zenith and azimuth angles. Black-sky surface albedo refers to a uni-directional incoming radiative flux, while white-sky surface albedo refers to diffuse incoming radiation.
Thermodynamic phase	The phase (liquid or ice) of cloud particles. The retrieved cloud phase product reflects the phase near the top of the cloud.